

1  
2  
3  
4  
5  
6  
7  
8  
9  
10  
11  
12  
13  
14  
15  
16  
17  
18  
19  
20  
21  
22  
23

# **A Bidirectional Switch in the Shank3 Phosphorylation State Biases Synapses toward Up or Down Scaling**

**Chi-Hong Wu<sup>1,2</sup>, Vedakumar Tatavarty<sup>1,2</sup>, Pierre MJ Beltran<sup>1,3</sup>, Andrea Guerrero<sup>2</sup>, Hasmik Keshishian<sup>3</sup>, Karsten Krug<sup>3</sup>, Melanie A MacMullan<sup>3</sup>, Li Li<sup>4</sup>, Steven A Carr<sup>3</sup>, Jeffrey R Cottrell<sup>4</sup>, and Gina G Turrigiano<sup>#,2</sup>**

<sup>1</sup> These authors contributed equally

<sup>2</sup> Dept of Biology, Brandeis University, Waltham, MA 02456

<sup>3</sup> Proteomics Platform, Broad Institute of MIT and Harvard, Cambridge MA 02142

<sup>4</sup> Stanley Center for Psychiatric Research, Broad Institute of MIT and Harvard,  
Cambridge MA 02142

<sup>#</sup> corresponding author

24 **ABSTRACT**

25 Homeostatic synaptic plasticity requires widespread remodeling of synaptic signaling  
26 and scaffolding networks, but the role of posttranslational modifications in this process has not  
27 been systematically studied. Using deepscale, quantitative analysis of the phosphoproteome  
28 in mouse neocortical neurons, we found wide-spread and temporally complex changes during  
29 synaptic scaling up and down. We observed 424 bidirectionally modulated phosphosites that  
30 were strongly enriched for synapse-associated proteins, including S1539 in the ASD-  
31 associated synaptic scaffold protein Shank3. Using a parallel proteomic analysis performed on  
32 Shank3 isolated from rat neocortical neurons by immunoaffinity, we identified two sites that  
33 were hypo-phosphorylated during scaling up and hyper-phosphorylated during scaling down:  
34 one (rat S1615) that corresponded to S1539 in mouse, and a second highly conserved site, rat  
35 S1586. The phosphorylation status of these sites modified the synaptic localization of Shank3  
36 during scaling protocols, and dephosphorylation of these sites via PP2A activity was essential  
37 for the maintenance of synaptic scaling up. Finally, phosphomimetic mutations at these sites  
38 prevented scaling up but not down, while phosphodeficient mutations prevented scaling down  
39 but not up. Thus, an activity-dependent switch between hypo- and hyperphosphorylation at  
40 S1586/ S1615 of Shank3 enables scaling up or down, respectively. Collectively our data show  
41 that activity-dependent phosphoproteome dynamics are important for the functional  
42 reconfiguration of synaptic scaffolds, and can bias synapses toward upward or downward  
43 homeostatic plasticity.

44

45

## 46 INTRODUCTION

47           Synaptic scaling is an important form of homeostatic plasticity that bidirectionally adjusts  
48 synaptic weights in response to prolonged perturbations in firing, in the correct direction to  
49 stabilize neuron and circuit activity (Turrigiano, 2008; Turrigiano et al., 1998; Turrigiano &  
50 Nelson, 2004). Synaptic scaling is expressed through changes in the postsynaptic  
51 accumulation of glutamate receptors that then lead to increases or decreases in postsynaptic  
52 strength. This form of plasticity is triggered by changes in calcium influx, transcription, and  
53 translation (Dörrbaum et al., 2020; Ibata et al., 2008; Mao et al., 2018; Schanzenbächer et al.,  
54 2016, 2018; Schaukowitch et al., 2017; Steinmetz et al., 2016) and involves a complex  
55 remodeling of the postsynaptic density that relies on a number of scaffolding and trafficking  
56 pathways within individual neurons (Gainey et al., 2015; Hu et al., 2010; Louros et al., 2018;  
57 Steinmetz et al., 2016; Sun & Turrigiano, 2011; Venkatesan et al., 2020). While synaptic  
58 scaling protocols are known to induce complex changes in the phosphoproteome (Desch et al.,  
59 2021), the causal roles these might play in homeostatic plasticity are largely unexplored. Here  
60 we show that synaptic scaling is accompanied by widespread and dynamic changes in the  
61 phosphoproteome that are especially enriched in synapse-associated proteins, and find that  
62 activity-dependent bidirectional changes in the phosphorylation state of the synaptic scaffold  
63 protein Shank3 are essential for the induction of synaptic scaling up and down.

64           Shank3 is a multidomain scaffold protein that is highly enriched at the postsynaptic  
65 density (Naisbitt et al., 1999) and interacts with a number of other scaffold and signaling  
66 proteins that are known to be important for synaptic scaling, such as Homer1 and the  
67 MAGUKs (Grabrucker et al., 2011; Jiang & Ehlers, 2013). Loss of function of human Shank3 is  
68 associated with autism spectrum disorders (ASDs), Phelan-McDermid syndrome, and

69 intellectual disability (Betancur & Buxbaum, 2013), indicating that Shank3 plays essential roles  
70 within the central nervous system. We recently showed that a cell-autonomous reduction in  
71 Shank3 is sufficient to completely abolish synaptic scaling up (Tatavarty et al., 2020), but how  
72 exactly Shank3 facilitates activity-dependent homeostatic changes in synaptic glutamate  
73 receptor abundance, and whether changes in phosphorylation state are important in this  
74 process, are unknown.

75         Here we employed liquid chromatography, tandem mass spectrometry (LC-MS/MS) to  
76 quantitatively profile changes in the synaptic phosphoproteome induced by scaling. We found  
77 widespread and temporally complex changes at many phosphosites (>2000 for scaling up and  
78 >3000 for scaling down), with strong enrichment for cytoskeletal and synapse-associated  
79 proteins. Of these phosphosites, 424 (representing 332 distinct proteins) were bidirectionally  
80 regulated during scaling up and down, including Shank3. Further analysis revealed two highly  
81 conserved adjacent sites on Shank3 (rat S1615 and rat S1586) that were persistently  
82 dephosphorylated during scaling up and were transiently hyperphosphorylated during scaling  
83 down. Dephosphorylation of Shank3 during scaling up was maintained by PP2A phosphatase  
84 activity, and reversing this dephosphorylation through PP2A inhibition also reversed synaptic  
85 scaling up. Finally, we found that mutating S1615 and S1586 to mimic (DD) phosphorylation  
86 blocked synaptic scaling up but not down, while mutating these sites to prevent (AA)  
87 phosphorylation blocked scaling down but not up. Taken together, these data show that  
88 hypophosphorylation of Shank3 through a PP2A-dependent process is essential for  
89 maintaining increased postsynaptic strength during scaling up, and suggest that the  
90 phosphorylation state of Shank3 can bias synapses toward upward or downward synaptic  
91 scaling.

92

## 93 **RESULTS**

### 94 **Synaptic scaling protocols induce widespread and dynamic changes in the** 95 **phosphoproteome**

96 While changes in phosphorylation of synaptic proteins such as glutamate receptors are  
97 thought to play a role in the expression of homeostatic plasticity (Diering & Huganir, 2018;  
98 Fernandes & Carvalho, 2016), the full range of activity-dependent phosphorylation changes  
99 induced by synaptic scaling paradigms have not been characterized. We designed an LC-  
100 MS/MS experiment to identify dynamic changes in the phosphoproteome during the prolonged  
101 increases and decreases in activity that drive homeostatic plasticity. Cultured mouse  
102 neocortical neurons were treated in biological duplicates with either tetrodotoxin (TTX, to block  
103 action potential firing) or bicuculline (BIC, to enhance firing) for 5 min, 1 hr, 7 hr, or 24 hr, in  
104 addition to a control untreated group. Following proteolytic digestion with trypsin and LysC, the  
105 peptides were labeled with isobaric mass tag reagents (TMT) to enable sample multiplexing  
106 and precise relative quantification. After mixing, samples were fractionated off-line and  
107 enriched for phosphopeptides prior to on-line LC-MS/MS to increase the depth of coverage of  
108 the proteome and phosphoproteome (Figure 1 – figure supplement 1A). A total of 31,840  
109 phosphosites and 9,643 proteins were quantified in the TTX-treated experiment, and 32,635  
110 phosphosites and 9,512 proteins were quantified in the BIC-treated experiment, altogether  
111 showing the high quality of this proteomics resource. Although biological replicates showed  
112 significant variance, the principal component analysis showed that replicate samples clustered  
113 together and followed the temporal progression of the experimental design (Figure 1 – figure  
114 supplement 1B, C).

115 Differential abundance analysis was performed using a moderated F-test, identifying  
116 proteins and phosphosites with a statistically significant response to BIC or TTX treatment  
117 throughout the time course (FDR adjusted p-value < 0.10) (Figure 1 – table supplement 1A-  
118 1D). No statistically significant changes in protein abundance were observed during TTX  
119 treatment, while 27 proteins were significantly regulated during BIC treatment (Figure 1 –  
120 figure supplement 1D, Figure 1 – table supplement 1A, C). These included transcriptional  
121 regulators (e.g., Junb, Jund, and Fos) that increased at later time points (7 and 24 hrs),  
122 suggesting long-term regulation of gene expression programs. In contrast to these modest  
123 changes in protein levels, the phosphoproteome data revealed widespread changes in  
124 phosphorylation, with 2,259 and 3,457 phosphosites regulated in response to TTX and BIC  
125 treatments, respectively (Figure 1A, B; Figure 1 – table supplement 1B, D).

126 These changes in the phosphoproteome were complex and dynamic (Figure 1A-C).  
127 Cluster analysis identified populations of phosphosites that increased or decreased during TTX  
128 treatment, with a range of temporal profiles; the BIC cluster analysis revealed similar  
129 complexity (Figure 1A, 1B, and 1C Top). To understand the biological processes regulated by  
130 these temporal profiles, we performed pathway enrichment analysis followed by network  
131 integration to summarize pathway enrichment results (Figure 1C Bottom, Figure 1 – table  
132 supplement 2). Neurogenesis pathways were enriched in proteins hyperphosphorylated and  
133 hypophosphorylated in response to TTX treatment (Figure 1C, Neurogenesis group), while  
134 neuron projection morphogenesis functions (involved in axon and dendrite formation and  
135 dynamics) were enriched in proteins hypophosphorylated in response to BIC (Figure 1C,  
136 Neuron Projection Morphogenesis group). Numerous pathways associated with synaptic  
137 signaling and the synaptic membrane were enriched in clusters that showed increases or

138 decreases during both TTX and BIC treatments (Figure 1C, Synaptic Signaling group).  
139 Cytoskeletal pathways were enriched only in phosphosites that increased in response to TTX  
140 (Cluster 3) and decreased in response to BIC (Cluster 4), suggesting that synaptic upscaling  
141 involves hyperphosphorylation of cytoskeletal components, and vice versa (Figure 1C,  
142 Cytoskeleton Organization group). Finally, splicing and RNA related processes were enriched  
143 in phosphosites with an early and strong hyperphosphorylation response to BIC (Figure 1C,  
144 Splicing and RNA Processing group), indicating gene expression regulation via  
145 phosphorylation during downscaling. We also observed enrichment of several developmental  
146 and morphogenesis pathways in BIC and TTX treatments. To facilitate visualization and  
147 exploration of regulated phosphoproteins and pathways in our dataset, we have made  
148 available web applications for browsing the TTX ([https://proteomics.broadapps.org/HSP\\_TTX/](https://proteomics.broadapps.org/HSP_TTX/))  
149 and BIC ([https://proteomics.broadapps.org/HSP\\_Bic/](https://proteomics.broadapps.org/HSP_Bic/)) proteomics data.

150         Synaptic scaling is a bidirectional process, with some overlap in the signaling pathways  
151 that regulate up- and downscaling (Fernandes & Carvalho, 2016). We noticed a large overlap  
152 of synapse-associated pathways across the BIC and TTX clusters. To gain more insight into  
153 the processes underlying synaptic scaling, we identified the 424 phosphosites that were  
154 bidirectionally regulated by TTX and BIC treatment when considering the average fold-change  
155 across all time points (Figure 1D, Figure 1 – table supplement 1E). The majority of these (335)  
156 were downregulated by TTX and upregulated by BIC, with a smaller number upregulated by  
157 TTX and downregulated by BIC (89). We hypothesized that these phosphosites could be  
158 prioritized for mechanistic characterization, as they may contribute to the bidirectional  
159 processes that underlie homeostatic changes in synaptic strength. These bidirectionally  
160 regulated phosphoproteins include the synaptic scaffold proteins Dbn1,Dlgap1, Dlgap4,

161 Homer2, Shank2, and Shank3; a number of neurotransmitter receptors and auxiliary proteins,  
162 including Grin3A, Grm5, Gabra2, Gabra5, and Shisa9; and several kinases important in  
163 cytoskeletal and synaptic plasticity, including Camk1d and Camk2b (Figure 1 – table  
164 supplement 1E). A number of motor, trafficking, and sorting proteins were also identified,  
165 including the adaptor protein complex AP3 Beta2 subunit (Ap3b2); enhanced expression of the  
166 AP3mu subunit was previously identified as an important factor in the routing of AMPAR to the  
167 synaptic membrane during scaling up (Steinmetz et al., 2016). Finally, a number of  
168 presynaptic proteins and ion channels were bidirectionally regulated during scaling (Figure 1 –  
169 table supplement 1E). While several of these regulated phosphoproteins have been previously  
170 implicated in synaptic scaling, one candidate in particular stood out to us: there were robust  
171 bidirectional changes in the phosphorylation state of Shank3 – an autism-associated synaptic  
172 scaffold protein known to be essential for synaptic scaling up - at S1539 (Figure 1E). These  
173 phosphorylation changes occurred without significant changes in protein abundance (Figure 1  
174 – table supplement 1A, C). We therefore prioritized Shank3 for in-depth characterization.

175

### 176 **Shank3 is bidirectionally phosphorylated in cultured rat neocortical neurons**

177 Our phosphoproteome screen identified Shank3 as a major synaptic scaffold protein  
178 that undergoes robust and bidirectional changes in phosphorylation during synaptic scaling  
179 protocols. Shank3 is essential for synaptic scaling up (Tatavarty et al., 2020), but it is unknown  
180 how Shank3 mediates synaptic plasticity, leading us to wonder whether activity-dependent  
181 changes in Shank3 phosphorylation might be critical drivers of synaptic scaling.

182 To address this question, we first examined whether these activity-dependent  
183 phosphorylation changes are conserved across two species (rats and mice) known to express



184 robust synaptic scaling. We isolated Shank3 protein from neurons cultured from postnatal rat  
185 visual cortex and analyzed by LC-MS/MS after 24 h TTX treatment or untreated controls  
186 (Figure 2A). We found an almost six-fold reduction in phosphorylation at residue rat S1615  
187 (Figure 2B). Sequence alignment analysis using Clustal Omega (Goujon et al., 2010;  
188 McWilliam et al., 2013; Sievers et al., 2011) showed that Shank3 is highly conserved, with rat  
189 Shank3 99.25% identical to its mouse homolog and human Shank3 94.62% and 95.66%  
190 identical to its rat and mouse homologs, respectively. Notably, the sequence around  
191 phosphosite S1615 is identical in rat and mouse, with S1615 corresponding to S1539 in mouse  
192 Shank3 (Figure 2C Bottom). Thus TTX induces a hypophosphorylation at this conserved site in  
193 both species. We identified a second residue, rat S1586, that was also hypophosphorylated by  
194 TTX treatment, albeit to a lesser extent (Figure 2B). Of note, S1586 and S1615 reside in the  
195 linker region between the proline-rich and the sterile-alpha-motif (SAM) domains of Shank3  
196 (Figure 2C Top).

197         Given that synaptic scaling is a process that unfolds over a time scale of many hours,  
198 we carefully explored the temporal dynamics of Shank3 phosphorylation. In mouse neocortical  
199 cultures, there was robust hypophosphorylation of S1539 that was rapidly expressed (within 10  
200 minutes) and persisted for up to 24 hours during continued TTX application (Figure 1E). In  
201 contrast, BIC treatment induced transient hyperphosphorylation at S1539 that was evident  
202 after 10 minutes but reversed within an hour (Figure 1E). A similar pattern was observed when  
203 Shank3 phosphorylation was assessed in rat cultures using an antibody against  
204 phosphorylated S1615 (pS1615, Figure 2 – figure supplement 1). Activity-blockade with TTX  
205 induced Shank3 hypophosphorylation at 10 minutes and 24 hours, while raising activity with  
206 picrotoxin (PTX, similar to BIC) induced transient hyperphosphorylation that reversed at 24 hr

207 (Figure 2D-G). Collectively, these data reveal activity-dependent, bidirectional modifications in  
208 the phosphorylation state of Shank3, and show that the temporal dynamics of these  
209 phosphorylation changes are conserved across species and culture conditions.

210

### 211 **Phosphorylation state modulates homeostatic changes in the synaptic enrichment of** 212 **Shank3**

213 Shank3 is highly enriched at the postsynaptic density, where it interacts with a number  
214 of synaptic scaffolding and signaling proteins that are important mediators of synaptic scaling  
215 (Gainey et al., 2015; Grabrucker et al., 2011; Hu et al., 2010; Jiang & Ehlers, 2013; Shin et al.,  
216 2012; Sun & Turrigiano, 2011). We asked whether synaptic scaling protocols might regulate  
217 the synaptic abundance of Shank3 by altering its phosphorylation state. Rat visual cortical  
218 cultures (used for all subsequent experiments) were treated with TTX or PTX for 24 hours,  
219 then fixed and labeled using antibodies against Shank3 and a surface epitope of the  
220 postsynaptic AMPA-type glutamate receptor GluA2 (sGluA2, Figure 3A), or the presynaptic  
221 glutamate transporter VGLUT1 (Figure 3D). Sites where Shank3 was colocalized with these  
222 postsynaptic (sGluA2) or presynaptic (VGLUT1) markers of excitatory synapses were identified,  
223 and the density of these sites along apical-like pyramidal neuron dendrites, as well as the  
224 intensity of the signals at these colocalized sites, were determined. Synaptic scaling protocols  
225 induced bidirectional changes in the synaptic accumulation of sGluA2, as expected (Figure 3A,  
226 B, Gainey et al., 2015; Iyata et al., 2008; Tatavarty et al., 2013); interestingly, activity blockade  
227 with TTX also increased, while enhancing activity with PTX reduced, the synaptic intensity of  
228 Shank3 (Figure 3A, C). Thus bidirectional changes in Shank3 synaptic abundance occur in  
229 tandem with the changes in AMPAR abundance that underlie synaptic scaling.

230 To evaluate whether the phosphorylation state of Shank3 influences its synaptic  
231 abundance, we generated expression constructs for Shank3 with double point mutations at  
232 residues S1586 and S1615, designed to mimic (DD mutants, where serine, S, was replaced  
233 with aspartic acid, D) or prevent (AA, where serine was replaced with alanine) phosphorylation  
234 at these sites (Figure 3D). We then expressed GFP-tagged wild-type, DD, or AA Shank3 at low  
235 efficiency in rat cultures, immunolabeled against VGluT1, and quantified the synaptic intensity  
236 of the GFP signal in pyramidal neuron apical-like dendrites. The density of colocalized puncta  
237 was not different between wildtype Shank3 and Shank3 mutants (Figure 3F). In contrast, there  
238 was a significant reduction in the accumulation of Shank3 DD at these colocalized sites  
239 relative to wildtype Shank3, while the AA mutant was slightly but not significantly increased  
240 (Figure 3E). These results show that the phosphomimetic Shank3 mutant accumulates less  
241 efficiently at synaptic sites and suggests that TTX-induced hypophosphorylation may  
242 contribute to the enhanced synaptic abundance of Shank3 during scaling up.

243

#### 244 **Increased PP2A activity maintains TTX-induced Shank3 hypophosphorylation.**

245 Neuronal activity could alter Shank3 phosphorylation by modulating kinase and/or  
246 phosphatase activity. Since scaling up is accompanied by robust and persistent  
247 hypophosphorylation of Shank3, we probed for the role of activity-dependent phosphatase  
248 activity in this hypophosphorylation. Protein phosphatase 2A (PP2A) plays an important role in  
249 some forms of synaptic plasticity (Colbran, 2004; Launey et al., 2004; Mauna et al., 2011;  
250 Winder & Sweatt, 2001; Woolfrey & Dell'Acqua, 2015); therefore, it seemed a likely candidate  
251 to dephosphorylate Shank3. We immunoprecipitated the catalytic unit of PP2A (PP2Ac) from  
252 cells treated with TTX and subjected it to an *in vitro* PP2A activity assay to detect any changes

253 in the activity of PP2A during scaling up. In comparison with untreated samples, we first  
254 observed a reduction in PP2A activity after one-hour TTX treatment (Figure 4A), which shifted  
255 to an increase after 24 hr treatment (Figure 4B).

256         These biphasic changes in phosphatase activity led us to hypothesize that PP2A may  
257 have a critical role in maintaining, rather than inducing, Shank3 hypophosphorylation during  
258 the late phase of scaling up. To test this idea, we treated cells with TTX for 1 or 24 hr, and  
259 during the last hour of the regimen, we applied okadaic acid (OKA), a phosphatase inhibitor  
260 that preferentially blocks PP2A activity at a low concentration (50 nM, Bialojan and Takai,  
261 1988; Cohen et al., 1989; Ishihara et al., 1989; Pribiag and Stellwagen, 2013). We then  
262 immunoprecipitated Shank3 and assessed the phosphorylation state of Shank3. As expected,  
263 inhibition of PP2A did not alter Shank3 hypophosphorylation in the early phase of scaling (one-  
264 hour TTX, Figure 4C, E); in contrast, the hypophosphorylation was reversed to baseline when  
265 OKA was introduced during the last hour of a 24-hour treatment with TTX (Figure 4D, F). We  
266 also observed a second band of phosphorylated Shank3 after OKA treatment, suggesting that  
267 there may be other phosphosites regulated by the OKA treatment that collectively induce a  
268 shift in molecule weight. OKA treatment alone did not alter the baseline phosphorylation level  
269 of Shank3, indicating that the role of PP2A in dephosphorylating Shank3 only manifested  
270 during prolonged neuronal inactivity (Figure 4E, F). We wondered whether other phosphatases  
271 such as protein phosphatase 1 (PP1) could also be involved in Shank3 phosphorylation, so we  
272 repeated this experiment using a higher concentration of OKA known to inhibit both PP2A and  
273 PP1 (500 nM, duBell et al., 2002; Ishihara et al., 1989; Pribiag and Stellwagen, 2013). Unlike  
274 PP2A, inhibition of PP1 resulted in significant hyperphosphorylation of Shank3 under baseline  
275 conditions (Figure 4 – figure supplement 1A, B). Taken together, these data suggest that PP1

276 controls baseline Shank3 phosphorylation, while PP2A undergoes an activity-dependent  
277 biphasic change in activity that maintains the hypophosphorylated state of Shank3 during  
278 activity blockade.

279

### 280 **PP2A is required for TTX-induced synaptic enrichment of Shank3.**

281 We next assessed whether PP2A activity influences the synaptic enrichment of Shank3  
282 during scaling up, using the more specific PP2A inhibitor fostriecin (FST, Walsh et al., 1997).  
283 Neurons were treated with TTX for 24 hours, and 10 nM FST was added during the final hour.  
284 Consistent with our previous dataset (Figure 3C), TTX treatment increased the intensity and  
285 density of synaptic Shank3 puncta (Figure 5A-C). Inhibition of PP2A prevented the increase in  
286 Shank3 puncta density (Figure 5C) and reduced (but did not eliminate) the increase in Shank3  
287 intensity at remaining Shank3 puncta (Figure 5B). FST treatment alone did not impact the  
288 baseline synaptic intensity or density of Shank3 puncta (Figure 5B, C), supporting the view that  
289 PP2A regulates phosphorylation and synaptic Shank3 localization only during activity  
290 blockade. We repeated this experiment with OKA and confirmed that PP2A inhibition  
291 diminished synaptic enrichment of Shank3 during activity blockade (Figure 5 – figure  
292 supplement 1A, B).

293 Because PP1 regulates Shank3 phosphorylation under basal conditions, we also tested  
294 whether PP1 inhibition influences synaptic Shank3 clustering by applying tautomycin  
295 (TAUT), a specific PP1 inhibitor (10 nM, Mitsuhashi et al., 2001). TAUT treatment alone  
296 reduced the baseline intensity of synaptic Shank3 without disrupting the density of synaptic  
297 Shank3 puncta (Figure 5D-F). Taken together with our direct measurements of Shank3  
298 phosphorylation (Figure 4C-F and Figure 4 – figure supplement 1), these data suggest that

299 PP1 influences baseline synaptic Shank3 clustering, while PP2A is recruited during activity  
300 deprivation to dephosphorylate Shank3 and promotes its enrichment at synapses.

301

302 **The phosphorylation state of Shank3 is critical for enabling bidirectional synaptic**  
303 **scaling.**

304 Shank3 is necessary for synaptic scaling up (Tatavarty et al., 2020), but whether  
305 changes in its phosphorylation state are critical for this (or indeed any other) function of  
306 Shank3 is unknown. To test this, we transfected neurons with our phosphomimetic (DD)  
307 mutant of Shank3 to determine whether preventing hypophosphorylation would block synaptic  
308 scaling up. We performed whole-cell patch-clamp recordings from transfected neurons and  
309 measured AMPAR-mediated miniature excitatory postsynaptic currents (mEPSCs), a  
310 physiological measure of postsynaptic strength. In neurons overexpressing Shank3 WT, TTX  
311 induced the normal increase in the mEPSC amplitude that is the classic measure of scaling up  
312 (Figure 6A, C). Strikingly, overexpression of the DD mutant completely blocked scaling up  
313 (Figure 6B, D), suggesting that dephosphorylation of Shank3 at these sites is essential for its  
314 induction.

315 While a normal complement of Shank3 is essential for scaling up (Tatavarty et al.,  
316 2020), whether it is also required for scaling down is unknown. To investigate this, we  
317 expressed a short-hairpin RNA at low efficiency to reduce synaptic Shank3 by ~50% in  
318 transfected pyramidal neurons (Tatavarty et al., 2020). Treatment of cultures with PTX for 24  
319 hr induced the expected reduction in mean mEPSC amplitude and a shift in the cumulative  
320 probability distribution of amplitudes toward smaller values (Figure 6 – figure supplement 1A,  
321 B), indicative of synaptic scaling down. Knockdown of Shank3 completely prevented scaling

322 down in transfected neurons (Figure 6 – figure supplement 1A, B), indicating that Shank3 is  
323 necessary for both directions of synaptic scaling. Because elevated neuronal activity induces  
324 transient hyperphosphorylation of S1615 (Figure 2D-G), we next wondered if this  
325 hyperphosphorylation was necessary for scaling down. Indeed, although scaling down was  
326 intact in neurons expressing WT Shank3, it was absent in neurons expressing the  
327 phosphodeficient AA mutant (Figure 6E-H).

328 Our data show that hypophosphorylation of Shank3 is necessary for scaling up, while  
329 hyperphosphorylation is necessary for scaling down. This suggests that the phosphorylation  
330 state of Shank3 acts as a switch to enable up or downscaling; if so, then scaling up should be  
331 intact in the AA (non-phosphorylatable) mutant, and scaling down should be intact in the DD  
332 (phosphomimetic) mutant. To test this, we transfected neurons with the AA mutant and treated  
333 them with TTX, or the DD mutant and treated with BIC, and then quantified synaptic GluA2 to  
334 measure synaptic scaling. We found that scaling up was indeed preserved in the AA mutant;  
335 likewise, scaling down was preserved in the DD mutant (Figure 6 – figure supplement 2);  
336 notably, expression of these mutants does not by itself drive scaling up or down, as baseline  
337 mEPSC amplitude was unaffected by AA or DD expression (Figure 6). Thus, phosphorylation  
338 of Shank3 at residues S1586 and S1615 blocks scaling up but is permissive for scaling down,  
339 while dephosphorylation at these same residues blocks scaling down but is permissive for  
340 scaling up.

341

### 342 **PP2A sustains scaling up through hypophosphorylation of Shank3.**

343 If the ability of PP2A inhibition to reverse scaling up is dependent upon enabling  
344 phosphorylation at S1586 and S1615 (Figure 4F), then it should be prevented by expression of



345 the AA mutant, which cannot be phosphorylated at these sites. To test this, we transfected  
346 neurons with either WT or AA Shank3, treated cultures with TTX for 24 hours, added FST  
347 during the last hour of treatment, and then measured synaptic scaling by quantifying the  
348 synaptic accumulation of GluA2. Compared with TTX treatment alone, we found that FST  
349 treatment significantly reduced synaptic sGluA2 intensity in cells expressing Shank3 WT  
350 (Figure 7A, B). In contrast, FST treatment was unable to reduce GluA2 accumulation in  
351 neurons expressing the AA mutant (Figure 7A, B). Similar to endogenous Shank3 (Figure 5B),  
352 the synaptic abundance of Shank3 WT was reduced upon FST treatment, while that of the AA  
353 mutant was not (Figure 7C). Taken together, these data demonstrate that PP2A maintains the  
354 expression of synaptic scaling up by dephosphorylating Shank3 at S1586 and S1615.

355

## 356 **DISCUSSION**

357 Homeostatic synaptic scaling is a bidirectional process that modifies the accumulation  
358 of synaptic glutamate receptors through a complex remodeling of postsynaptic scaffolding,  
359 trafficking, and signaling networks (Gainey et al., 2015; Hu et al., 2010; Louros et al., 2018;  
360 Steinmetz et al., 2016; Sun & Turrigiano, 2011; Tataavarty et al., 2020; Venkatesan et al.,  
361 2020). Notably, scaling up and down have been reported to support the therapeutic effects of  
362 ketamine and lithium on depression and bipolar disorder, respectively; thus, a complete  
363 understanding of how synaptic scaling is regulated bidirectionally could potentially help  
364 advance targeted treatments of these mood disorders (Kavalali & Monteggia, 2020). While  
365 transcriptional and translational regulation of this process has been intensively studied, it  
366 remains unclear which causal role(s) posttranslational modifications play. Here we analyzed  
367 the temporal dynamics of the phosphoproteome during the prolonged changes in activity that



368 drive synaptic scaling up and down and found widespread and dynamic regulation of  
369 phosphorylation that was especially enriched in pathways related to synaptic scaffolding and  
370 signaling. We then focused on Shank3, a synaptic scaffold protein known to be essential for  
371 synaptic scaling (Tatavarty et al., 2020), and which exhibited robust and bidirectional changes  
372 in phosphorylation during scaling protocols. We found that Shank3 is dephosphorylated at two  
373 sites (S1586 and S1615) during scaling up and hyperphosphorylated during scaling down.  
374 These changes in phosphorylation modified the synaptic localization of Shank3 during scaling  
375 and were necessary for its expression. Finally, we found that dephosphorylation of these sites  
376 via PP2A activity was essential for the maintenance of synaptic scaling up. These data show  
377 that Shank3 undergoes an activity-dependent switch between hypo- and hyperphosphorylation  
378 at S1586/ S1615 that is necessary to enable scaling up or down, respectively. More broadly,  
379 widespread changes in the phosphoproteome are likely to be instrumental in reconfiguring pre-  
380 and postsynaptic scaffold and signaling pathways during homeostatic plasticity.

381 Mass spectrometry-based proteomics has been successful in elucidating  
382 phosphorylation signaling and adaptation mechanisms in various forms of synaptic plasticity  
383 (Guan et al., 2011; Hwang et al., 2021; Li et al., 2016). In this work, we began by exploring  
384 changes induced by homeostatic scaling protocols, using a quantitative proteomic and  
385 phosphoproteomic methodology. The multiplexing strategy and extensive peptide fractionation  
386 provided deep coverage of proteins and phosphosites while reducing technical variability. We  
387 identified over 5200 temporally regulated phosphosites (FDR adjusted p-value < 0.10), with  
388 only subtle changes in protein levels: only 27 proteins in the BIC treatment condition showed  
389 differential abundance changes with our statistical significance criteria. Dörrbaum et al.  
390 previously characterized the proteome synthesis, degradation, and turnover during

391 homeostatic scaling (Dörrbaum et al., 2020). Their work identified hundreds of proteins with  
392 differential abundance during 7 days of treatment; the longer treatment conditions and higher  
393 number of replicates they used may be necessary to capture these relatively modest  
394 abundance changes. Nonetheless, our work shows that extensive phosphorylation events with  
395 large effect sizes occur at a point in time (24 hr) when there is robust synaptic scaling and  
396 relatively small changes in protein abundance. Importantly, 424 of these phosphosites –  
397 including Shank3 – exhibited bidirectional changes in phosphorylation during scaling up and  
398 down. The global pattern of change in the phosphoproteome during synaptic scaling up and  
399 down, and the enrichment in pathways related to synaptic scaffolding and signaling, is  
400 consistent with a recent study that used a label-free MS approach (Desch et al., 2021). Thus  
401 synaptic scaling results in widespread bidirectional regulation of the phosphoproteome, and  
402 these changes may contribute to the regulation of a wide range of cell-biological processes  
403 that contribute to the expression of homeostatic plasticity.

404 In addition to synaptic scaling of excitatory synapses, prolonged changes in activity  
405 produce a wide range of homeostatic network adaptations that include changes in intrinsic  
406 excitability and inhibition (Turrigiano, 2011). Proteomics revealed a number of voltage-gated  
407 ion channel subunits that are differentially phosphorylated during scaling up and down  
408 protocols that are candidate contributors to these intrinsic excitability changes (Figure 1 – table  
409 supplement 1). These ion channels include hyperpolarization-activated cyclic nucleotide-gated  
410 (HCN) channels (Hcn1 and Hcn2), delayed rectifier and inwardly rectifying potassium channel  
411 subunits (Kcnb1 and Kcnj3), and L and T type calcium channel subunits (Cacna1c and  
412 Cacna1i). The function of phosphorylation at the sites identified on these channel subunits will  
413 be an interesting avenue of exploration for understanding the mechanisms of intrinsic

414 homeostatic plasticity. Similarly, we identified changes in phosphorylation in a network of  
415 presynaptic scaffold and release proteins including Bassoon (Bsn), Piccolo (Pclo), Synapsin 2  
416 and 3 (Syn2 and Syn3), and Synaptotagmin 11 and 17 (Syt11 and Syt17), that may contribute  
417 to presynaptic adaptations. Coupled with the widespread changes in postsynaptic scaffolding  
418 and signaling proteins (including Dlgap1 and 4, Homer2, Shank2, Shank3, and Shisa9), these  
419 data support the notion of coordinated pre- and postsynaptic adaptations during synaptic  
420 scaling. Finally, we identified bidirectional changes in phosphorylation of a number of  
421 neurotransmitter receptors known to be important for inhibitory and excitatory homeostatic  
422 plasticity, including the GABA<sub>A</sub>R subunits Gabra2 and Gabra5, the NMDAR subunit Grin3A,  
423 and the mGluR5 subunit Grm5. In contrast, although bidirectional changes in phosphorylation  
424 of GluA2 at Y876 has been reported after 48 hr of activity manipulation (Yong et al., 2020), we  
425 failed to detect such changes; this may reflect the shorter treatment times used here (24 rather  
426 than 48 hr) and underscores the dynamic nature of activity-dependent phosphorylation events.  
427 Although we have focused our attention here on sites that undergo bidirectional  
428 phosphorylation, it is important to note that the machinery that drives scaling up and down (and  
429 possibly other forms of homeostatic plasticity) are not entirely overlapping (for scaling up  
430 specific examples, see Stellwagen & Malenka, 2006; Tan et al., 2015; for scaling down  
431 examples, see Sun & Turrigiano, 2011; Wang et al., 2017), and so some of the large number  
432 of unidirectionally affected phosphosites we identified may also prove to be mechanistically  
433 important.

434 Changes in the phosphorylation state of Shank3 were of particular interest to us since  
435 Shank3 is critical for synaptic scaling up (Tatavarty et al., 2020), interacts with many synaptic  
436 partners also known to be important for homeostatic plasticity (Gainey et al., 2015; Hu et al.,

437 2010; Shin et al., 2012), and is strongly associated with ASDs and intellectual disability  
438 (Betancur & Buxbaum, 2013). We found that Shank3 is bidirectionally phosphorylated during  
439 scaling on two conserved sites in the linker region between the proline-rich and SAM domains  
440 in both mouse and rat neocortical neurons and that these phosphorylation changes showed  
441 similar dynamics between species, with immediate and prolonged dephosphorylation induced  
442 by activity-deprivation, and transient early hyperphosphorylation when activity is raised. One of  
443 these sites (reported as S1511, corresponding to rat S1586 in our dataset) was also identified  
444 in Desch et al.'s report, while rat S1615 was not (Desch et al., 2021). This likely reflects more  
445 comprehensive coverage of Shank3 in our assays. These changes in phosphorylation state  
446 gate changes in the synaptic abundance of Shank3 during scaling and are essential for the  
447 expression of synaptic scaling up and down (respectively). The different time courses of  
448 Shank3 phosphorylation changes during scaling up and down are intriguing and suggest that  
449 the temporal dynamics of the synaptic scaling machinery are more complex than previously  
450 appreciated. In particular, while the transient hyperphosphorylation of Shank3 is necessary to  
451 initiate scaling down, it need not be maintained for the subsequent slow removal of synaptic  
452 AMPAR that underlies the reduction in synaptic strength. In contrast, upscaling requires the  
453 continuous and active hypophosphorylation of Shank3, as transiently reversing this  
454 hypophosphorylation after 24 hr of scaling by inhibiting PP2A rapidly reverses scaling up.

455 Activity-dependent changes in Shank3 phosphorylation could be achieved through the  
456 altered activity of kinases, phosphatases, or both. Several activity-dependent kinases are  
457 known to regulate Shank3: ERK2 and its downstream target ribosome S6 kinase (RSK)  
458 phosphorylate Shank3 at S1134/S1163/S1253 (Wang et al., 2020a) and S1648 (Thomas et al.,  
459 2005), respectively, while CaMKII can target S782 (Jeong et al., 2021) and S1586 (Dosemeci

460 & Jaffe, 2010). Moreover, both CaMKII and PKA can phosphorylate S685 (Perfitt et al., 2020;  
461 Wang et al., 2020b), highlighting the complexity of the kinase network that could potentially  
462 regulate Shank3 phosphorylation. In addition to being a target of multiple kinases, Shank3  
463 dephosphorylation is actively maintained by phosphatases: we found that PP1 modulates  
464 basal levels of Shank3 phosphorylation, while PP2A undergoes a delayed increase in activity  
465 upon TTX treatment that is required to maintain the hypophosphorylated state of Shank3  
466 during late scaling. One model that could explain these temporal dynamics during scaling up  
467 is that reduced kinase (such as ERK2) activity may account for the early stage of Shank3  
468 hypophosphorylation, which is then maintained by the delayed activation of PP2A.

469         How does the phosphorylation state of Shank3 enable scaling up and down? Our  
470 observation that phosphorylation at S1586/ S1615 influences synaptic enrichment of Shank3  
471 suggests that this phosphorylation contributes to the recruitment and/or stability of Shank3 at  
472 the synapse. This connection between Shank3 phosphorylation and synaptic clustering is  
473 supported by the recent observation that dephosphorylation at S782 increases the synaptic  
474 enrichment of Shank3 (Jeong et al., 2021). S1586 and S1615 are located in the linker region  
475 between the proline-rich domain and the SAM domain. The SAM domain promotes synaptic  
476 targeting (Boeckers et al., 2005), oligomerization, and stabilization of Shank3 (Baron et al.,  
477 2006; Hayashi et al., 2009; Naisbitt et al., 1999), suggesting that phosphorylation at these sites  
478 might influence synaptic Shank3 enrichment by regulating the function of the SAM domain.  
479 The proximity of S1586 and S1615 to the upstream proline-rich domain, which interacts with  
480 important cytoskeletal and signaling elements including cortactin and Homer1 (Naisbitt et al.,  
481 1999), also raises the possibility that the phosphorylation state of these sites modulates the  
482 interaction of Shank3 with local signaling pathways essential for synaptic plasticity.

483 Shank3 is a complex, multiply phosphorylated protein that is highly enriched in the  
484 postsynaptic density and interacts both directly and indirectly with cytoskeletal elements,  
485 synaptic scaffold proteins, glutamate receptors, and synaptic signaling elements (Grabrucker  
486 et al., 2011; Jiang & Ehlers, 2013). Shank3 is thus perfectly placed to act as a signaling and  
487 scaffolding hub that can coordinate the activity of the multiple cell-biological processes  
488 required to drive homeostatic increases and decreases in synaptic strength. Taken together,  
489 our data show that bidirectional and temporally complex changes in Shank3 phosphorylation  
490 are necessary for synaptic scaling, and suggest that the function of Shank3 within the  
491 postsynaptic density is dynamically modulated by its phosphorylation state to switch it from a  
492 configuration that promotes scaling up to one that promotes scaling down. This has important  
493 implications for our understanding of bidirectional synaptic plasticity, and how loss of Shank3  
494 contributes to synaptic and circuit dysfunction.

495

## 496 MATERIALS AND METHODS

497 All animal procedures were performed according to NIH guidelines and were approved  
498 by the Broad Institute of MIT and Harvard IACUC (mouse cultures) or the Brandeis University  
499 IACUC (rat cultures).

500

## 501 Key Resources Table

Reagent type (species) or resource	Designation	Source or reference	Identifiers	Additional information
strain, strain background (Rattus norvegicus)	Long-Evans	Charles River Laboratories	Strain: 006; RRID: RGD_2308852	
strain, strain background (Mus musculus)	C57BL/6	Charles River Laboratories	Strain:027; RRID: IMSR_CRL:27	
antibody	Guinea pig anti-Shank3 (polyclonal)	Synaptic Systems	Cat#: 162 304; RRID: AB_2619863	IF (1:1000); WB (1:1000)

antibody	Rabbit anti-pS1615 (polyclonal)	this paper		WB (1:1000)
antibody	Rabbit anti-HA (monoclonal), C29F4	Cell Signaling Technology	Cat#:3724S; RRID: AB_1549585	IP (1:500)
antibody	Chicken anti-HA (polyclonal)	Aves Labs	Cat#: ET-HA100; RRID: AB_2313511	WB (1:1000)
antibody	Donkey anti-rabbit IRDye 680RD	LI-COR	Cat#: 925-68073; RRID: AB_2716687	WB (1:5000)
antibody	Donkey anti-guinea pig IRDye 800CW	LI-COR	Cat#: 925-32411; RRID: AB_2814905	WB (1:5000)
antibody	Donkey anti-chicken IRDye 800CW	LI-COR	Cat#: 925-32218; RRID: AB_2814922	WB(1:5000)
antibody	Chicken anti-GFP (polyclonal)	Aves Labs	Cat#: GFP-1020; RRID: AB_2307313	IF (1:1000)
antibody	Guinea pig anti-VGluT1 (polyclonal)	Synaptic Systems	Cat#: 135 304; RRID: AB_887878	IF (1:1000)
antibody	Rabbit anti-VGluT1 (polyclonal)	Synaptic Systems	Cat#: 135 302; RRID: AB_887877	IF (1:1000)
antibody	Mouse anti-GluA2 (monoclonal)	gift from Eric Gouaux, OHSU		IF (1:1000)
antibody	Goat anti-chicken Alexa 488 (polyclonal)	Thermo Fisher Scientific	Cat#: A-11039; RRID: AB_142924	IF (1:400)
antibody	Goat anti-mouse Alexa 555 (polyclonal)	Thermo Fisher Scientific	Cat#: A-21424; RRID: AB_141780	IF (1:400)
antibody	Goat anti-guinea pig Alexa 555 (polyclonal)	Thermo Fisher Scientific	Cat#: A-21435; RRID: AB_2535856	IF (1:400)
antibody	Goat anti-guinea pig Alexa 647 (polyclonal)	Thermo Fisher Scientific	Cat#: A-21450; RRID: AB_2735091	IF (1:400)
antibody	Goat anti-rabbit Alexa 647 (polyclonal)	Thermo Fisher Scientific	Cat#: A-21245; RRID: AB_2535813	IF (1:400)
recombinant DNA reagent	Shank3 Short Hairpin (PVLTHM)	gift from Chiara Verpelli		Verpelli et al., 2011
recombinant DNA reagent	pDEST53-CMV-Cycle3GFP-Shank3 WT (short-hairpin insensitive)	gift from Chiara Verpelli		Verpelli et al., 2011
recombinant DNA reagent	pDEST53-CMV-Cycle3GFP-Shank3 S1586A/S1615A	this paper		5' <i>gcattggggagggaaccagtggtggcctgggtagcctgctggaccctgctaagaagtcgccattgcagcagctcgctctcagcga</i> 3'
recombinant DNA reagent	pDEST53-CMV-Cycle3GFP-Shank3 S1586D/S1615D	this paper		5' <i>gactggggagggaaccagtggtggcctgggtagcctgctggaccctgctaagaagtcgccattgcagcagctcgctctcagcac</i> 3'
recombinant DNA reagent	pDEST53-CMV-HA-Shank3 WT	this paper		
recombinant DNA reagent	pDEST53-CMV-HA-Shank3 S1586A/S1615A	this paper		
recombinant DNA reagent	pAAV-CMV-PI-EGFP-WPRE-bGH	gift from James M. Wilson	Addgene#: 105530; RRID: Addgene_105530	
commercial assay or kit	Lipofectamine 2000	Thermo Fisher Scientific	Cat#: 11668-027	
commercial assay or kit	Gibson Assembly Master Mix	New England Biolabs	Cat#: E2611S	
commercial assay or kit	Lambda protein phosphatase	New England Biolabs	Cat#: P0753S	
commercial assay or kit	BCA Protein Assay Kit	Thermo Fisher Scientific	Cat#: 23227	
commercial assay or kit	Protein-G Magnetic Beads	Thermo Fisher Scientific	Cat#: 88847	



commercial assay or kit	SimplyBlue SafeStain	Thermo Fisher Scientific	Cat#: LC6060	
commercial assay or kit	PP2A Immunoprecipitation Phosphatase Assay Kit	Millipore	Cat#: 17-313	
commercial assay or kit	Ni-NTA Superflow Agarose Beads	Qiagen	Cat#: 30410	
chemical compound, drug	Tetrodotoxin	Tocris	Cat#: 1069	
chemical compound, drug	Bicuculline methobromide	Tocris	Cat#: 0109	
chemical compound, drug	Picrotoxin	Sigma-Aldrich	Cat#: P1675	
chemical compound, drug	Okadaic acid	Santa Cruz	Cat#: sc-3513	
chemical compound, drug	Tautomycetin	Tocris	Cat#: 2305	
chemical compound, drug	Fostriecin	Tocris	Cat#: 1840	
chemical compound, drug	Sequencing-grade trypsin	Promega	Cat#: V5111	
chemical compound, drug	Tandem Mass Tag (TMT) 10plex	Thermo Fisher Scientific	Cat#: 90110	
software, algorithm	Image Lab Software	Bio-Rad	RRID:SCR_014210	<a href="https://www.bio-rad.com/en-us/product/image-lab-software?ID=KRE6P5E8Z&amp;source_wt=imageIabsoftware_surl">https://www.bio-rad.com/en-us/product/image-lab-software?ID=KRE6P5E8Z&amp;source_wt=imageIabsoftware_surl</a>
software, algorithm	ZEN Black	Zeiss	RRID:SCR_018163	<a href="https://www.zeiss.com">https://www.zeiss.com</a>
software, algorithm	Metamorph	Molecular Devices	RRID:SCR_002368	<a href="http://www.moleculardevices.com/Products/Software/Meta-Imaging-Series/MetaMorph.html">http://www.moleculardevices.com/Products/Software/Meta-Imaging-Series/MetaMorph.html</a>
software, algorithm	FIJI	FIJI	RRID:SCR_002285	<a href="http://fiji.sc">http://fiji.sc</a>
software, algorithm	GraphPad Prism	GraphPad	RRID:SCR_002798	<a href="http://www.graphpad.com/">http://www.graphpad.com/</a>
software, algorithm	IGOR pro	Wavemetrics	RRID:SCR_000325	<a href="https://www.wavemetrics.com/products/igorpro/igorpro.htm">https://www.wavemetrics.com/products/igorpro/igorpro.htm</a>
software, algorithm	Spectrum mill v.7.00.208	Agilent Technologies		
software, algorithm	R v 4.0	The R Foundation	RRID:SCR_001905	<a href="https://www.R-project.org/">https://www.R-project.org/</a>
software, algorithm	Cytoscape v 3.8.2	Cytoscape	RRID:SCR_003032	<a href="http://cytoscape.org">http://cytoscape.org</a>
software, algorithm	EnrichmentMap	EnrichmentMap	RRID:SCR_016052	<a href="http://baderlab.org/Software/EnrichmentMap">http://baderlab.org/Software/EnrichmentMap</a>
other	Odyssey Blocking Buffer	LI-COR	Cat#: 927-40000	
other	DAPI-Fluoromount-G	SouthernBiotech	Cat#: 0100-20	



## 503 **Neuronal Cultures, Transfections and Drug Treatments**

504 ***Rat cultures:*** Timed-pregnant Long-Evans rats were obtained from Charles River.  
505 Primary neuronal cultures were dissociated from the visual cortex of newborn pups (postnatal  
506 day1-3) and plated onto glass-bottomed dishes pre-seeded with glial feeders as previously  
507 described (Gainey et al., 2015; Tatavarty et al., 2020). All the experiments were performed  
508 from 7 to 10 days in vitro (DIV), during which neurons were sparsely transfected with the  
509 following constructs using lipofectamine 2000 (Thermo Fisher Scientific). To exogenously  
510 express Shank3 phospho-mutants, Shank3 constructs (2500 ng per dish) were transfected. To  
511 knock down endogenous Shank3, an shRNA targeting Shank3 (Tatavarty et al., 2020; Verpelli  
512 et al., 2011) was used. For better visualization of neurons during recording, an empty GFP  
513 vector was co-transfected in both conditions. In the imaging experiments that measured  
514 endogenous Shank3, an empty GFP vector (500 ng per dish) was transfected to delineate the  
515 neurons. To induce scaling up, 6 hrs (Figure 6 – figure supplement 2) or 24 hrs after  
516 transfection (the remaining experiments) neurons were treated with tetrodotoxin (TTX, 5  $\mu$ M,  
517 Tocris) for ~16 hours. To induce scaling down, picrotoxin (PTX, 100  $\mu$ M, Sigma-Aldrich) or  
518 bicuculline (BIC, 20  $\mu$ M, Tocris) were used for the same duration. In the experiments where  
519 phosphatases were inhibited, okadaic acid (50 nM or 500 nM, Santa Cruz), fostriecin (10 nM,  
520 Tocris), or tautomycetin (10 nM, Tocris) were introduced during the last hour of the scaling-  
521 inducing regimen. Because the phosphatase inhibitors were dissolved in DMSO, the same  
522 volume of DMSO was added to matched sister cultures for the same duration as controls. For  
523 western blotting and mass spectrometry, dissociated neurons were plated onto 10-cm plates  
524 without the glial feeders and underwent the same treatments described above.

525           **Mouse cultures:** Timed pregnant C57BL/6 mice were acquired from Charles River.  
526 Tissue collection was performed at E17. Cortex was dissected in ice-cold Hibernate E medium  
527 (Thermo Fisher Scientific) supplemented with 2% B27 supplement (Thermo Fisher Scientific)  
528 and 1% Pen/Strep (Thermo Fisher Scientific). Brain tissues were digested in Hibernate E  
529 containing 20 U/mL papain, 1 mM L-cysteine, 0.5 mM EDTA (Worthington Biochem kit), and  
530 0.01% DNase (Sigma-Aldrich) for 10 min. Neurons were dissociated and plated at a density of  
531  $6 \times 10^6$ /dish onto poly-D-lysine coated 100 mm plates (Biocoat, Corning). Cortical neurons  
532 were seeded and maintained in NbActiv1 (BrainBits Inc, Springfield, IL) and grown at 37 °C in  
533 95% air with 5% CO<sub>2</sub> humidified incubator for 16 days. Cortical neurons were left untreated for  
534 control or treated with 1 μM TTX or 20 μM Bicuculline for 5 min, 1 hr, 7 hr, and 24 hr before  
535 collection for proteomics and phosphoproteomics analysis.

536

### 537 **Proteomic Profiling of Mouse Neuronal Cultures**

538           **In-solution digestion:** Neuronal cell pellets containing  $\sim 6.6 \times 10^6$  cells were lysed for 30  
539 min at 4 °C in urea lysis buffer (8M urea, 50 mM Tris-HCl pH 8.0, 75 mM NaCl, 1 mM EDTA, 2  
540 μg/μl aprotinin (Sigma-Aldrich), 10 μg/μl leupeptin (Roche), 1 mM phenylmethylsulfonyl fluoride  
541 (PMSF) (Sigma-Aldrich), 10mM NaF, and 1:100 phosphatase inhibitor cocktails 2 and 3  
542 (Sigma-Aldrich)) and cleared by centrifugation at 20,000 x g. Samples were reduced with 5  
543 mM dithiothreitol (DTT) for 1 h at 25°C, followed by alkylation with 10 mM iodoacetamide for 45  
544 min at 25°C. Samples were diluted with 50 mM Tris-HCl pH 8.0 to a final urea concentration of  
545 2 M preceding enzymatic digestion. Proteins were digested with endoproteinase LysC (Wako  
546 Laboratories) for 2 h at 25 °C followed by overnight digest with sequencing-grade trypsin  
547 (Promega) at 25 °C (enzyme-to-substrate ratios of 1:50). Following digestion, samples were

548 acidified to a concentration of 1% formic acid (FA) and cleared by centrifugation at 20,000 rcf.  
549 Remaining soluble peptides were desalted using a reverse phase tC18 SepPak cartridge  
550 (Waters). Cartridges were conditioned with 1 ml 100% acetonitrile (MeCN) and 1 ml 50%  
551 MeCN/0.1% FA, then equilibrated with 4X 1 ml 0.1% trifluoroacetic acid (TFA). Samples were  
552 loaded onto the cartridge and washed 3X with 1 ml 0.1% TFA and 1X with 1 ml 1% FA, then  
553 eluted with 2X 600  $\mu$ l 50% MeCN/0.1% FA. Samples were dried down by vacuum  
554 centrifugation, then reconstituted, and their concentrations were measured by BCA assay. 400  
555  $\mu$ g aliquots were made based on the peptide level concentration for TMT labeling.

556 ***TMT labeling of peptides:*** TMT labeling was performed as previously described  
557 (Zecha et al., 2019). Briefly, 400  $\mu$ g of peptides per sample were resuspended in 50 mM  
558 HEPES pH 8.5 at a concentration of 5 mg/ml. Dried Tandem Mass Tag (TMT) 10-plex reagent  
559 (Thermo Fisher Scientific) was reconstituted at 20  $\mu$ g/ $\mu$ l in 100% anhydrous MeCN and added  
560 to samples at a 1:1 TMT to peptide mass ratio. The reaction was incubated for 1 hr at 25 °C  
561 while shaking and quenched with 5% hydroxylamine to a final concentration of 0.2% for 15 min  
562 at 25 °C while shaking. The TMT-labeled samples were then combined, dried to completion by  
563 vacuum centrifugation, reconstituted in 1 ml 0.1% FA, and desalted with a 100 mg SepPak  
564 cartridge as described above.

565 ***Basic Reverse Phase (bRP) fractionation:*** TMT-labeled peptides were fractionated  
566 via offline basic reverse-phase (bRP) chromatography as previously described (Mertins et al.,  
567 2018). Chromatography was performed with a Zorbax 300 Extend-C18 column (4.6 x 250 mm,  
568 3.5  $\mu$ m, Agilent) on an Agilent 1100 high pressure liquid chromatography (HPLC) system.  
569 Samples were reconstituted in 900  $\mu$ l of bRP solvent A (5 mM ammonium formate, pH 10.0 in  
570 2% vol/vol MeCN). Peptides were separated at a flow rate of 1ml/min in a 96 min gradient with

571 the following concentrations of solvent B (5 mM ammonium formate, pH 10.0 in 90% vol/vol  
572 MeCN) 16%B at 13 min, 40%B at 73 min, 44%B at 77 min, 60%B at 82 min, 60%B at 96 min.  
573 A total of 96 fractions were collected and concatenated non-sequentially into 24 fractions. A  
574 total of 5% of each of the 24 fractions was reserved for global proteome analysis. The  
575 remaining 95% of each fraction were concatenated into 13 fractions for metal affinity  
576 chromatography and phosphoproteome analysis.

577 ***Metal affinity chromatography:*** Ni-NTA Superflow Agarose Beads (Qiagen) were  
578 prepared for metal affinity enrichment by performing 3x washes in HPLC water, 1x 30 min  
579 incubation in 100 mM EDTA, 3x washes in HPLC water, 1x 30 min incubation in 10 mM FeCl<sub>3</sub>  
580 in water (Sigma), and 3x washes in HPLC water. The beads were centrifuged to remove  
581 supernatant and resuspended in 1:1:1 Acetonitrile: Methanol: 0.01% Acetic Acid solvent prior  
582 to incubation with peptides. Dried peptides were resuspended in 80% MeCN/0.1% TFA at a  
583 concentration of 0.5 µg/µL and incubated with 10 µL of beads for 30 min at room temperature  
584 with gentle end-over-end mixing and then centrifuged briefly to remove the flowthrough. The  
585 beads with phosphopeptides bound were transferred on top of a stage tip containing 2X C18  
586 (Empore) discs and washed 3x with 100 µL of 80%MeCN/0.1%TFA and 1x with 50 µl 1% FA  
587 by centrifugation. Peptides were eluted from the beads and bound to the C18 discs using 225  
588 µL IMAC elution buffer (500 mM K<sub>2</sub>HPO<sub>4</sub>, pH 7). Stage-tip desalting was performed with 1x  
589 100 µL 1%FA in water and eluted with 50 µL of 50%ACN/0.1%FA in water. Peptides were  
590 dried by vacuum centrifugation.

591 ***Liquid chromatography and mass spectrometry:*** Dried fractions were reconstituted  
592 in 3% MeCN/0.1% FA to an estimated peptide concentration of 1 µg/µl for global proteome or  
593 by adding 8 µL per fraction for phosphoproteome fractions. Peptides were analyzed via

594 coupled nanoflow liquid chromatography and tandem mass spectrometry (LC-MS/MS) using a  
595 Proxeon Easy-nLC 1000 (Thermo Fisher Scientific) coupled to an Orbitrap Q-Exactive Plus  
596 Mass Spectrometer (Thermo Fisher Scientific). A sample load of 1 µg (global proteome) or half  
597 of the available sample (phosphoproteome) for each fraction was separated on a capillary  
598 column (360 x 75 µm, 50 °C) containing an integrated emitter tip packed to a length of  
599 approximately 25 cm with ReproSil-Pur C18-AQ 1.9 µm beads (Dr. Maisch GmbH).  
600 Chromatography was performed with a 110 min gradient of solvent A (3% MeCN/0.1% FA)  
601 and solvent B (90% MeCN/0.1% FA). The gradient profile, described as min:% solvent B, was  
602 0:2, 1:6, 85:30, 94:60, 95:90, 100:90, 101:50, 110:50. Ion acquisition was performed in data-  
603 dependent acquisition mode with the following relevant parameters: MS1 orbitrap acquisition  
604 (70,000 resolution, 3E6 AGC target, 5ms max injection time) and MS2 orbitrap acquisition (top  
605 12, 1.6m/z isolation window, 30% HCD collision energy, 35,000 resolution, 5E4 AGC target,  
606 120 ms max injection time, 2.1E4 intensity threshold, 20s dynamic exclusion). The original  
607 mass spectra and the protein sequence databases used for searches have been deposited in  
608 the public proteomics repository MassIVE (<http://massive.ucsd.edu>) and are accessible at  
609 <ftp://MSV000087926@massive.ucsd.edu>.

610 **MS Data Processing:** MS/MS data was analyzed using Spectrum Mill v.7.00.208  
611 (Agilent Technologies). MS2 spectra were extracted from RAW files and merged if originating  
612 from the same precursor, or within a retention time window of +/- 60 s and m/z range of +/- 1.4,  
613 followed by filtering for precursor mass range of 750-6000 Da and sequence tag length > 0.  
614 MS/MS search was performed against the mouse UniProt protein database downloaded on  
615 April 2021 and common contaminants, with digestion enzyme conditions set to “Trypsin allow  
616 P”, <5 missed cleavages, fixed modifications (cysteine carbamidomethylation and TMT10 on

617 N-term and internal lysine), and variable modifications (oxidized methionine, acetylation of the  
618 protein N-terminus, pyroglutamic acid on N-term Q, and pyro carbamidomethyl on N-term C).  
619 For phosphoproteome analysis, phosphorylation of S, T, and Y were added to the variable  
620 modifications. Matching criteria included a 30% minimum matched peak intensity and a  
621 precursor and product mass tolerance of +/- 20 ppm. Peptide-level matches were validated at  
622 a 0.8% false discovery rate (FDR) threshold and within a precursor charge range of 2-6. A  
623 second round of validation was then performed for protein-level matches, requiring a minimum  
624 protein score of 13 for the global proteome dataset. TMT10 reporter ion intensities were  
625 corrected for isotopic impurities in the Spectrum Mill protein/peptide summary module using  
626 the afRICA correction method which implements determinant calculations according to  
627 Cramer's Rule (Shadforth et al., 2005) and correction factors obtained from the reagent  
628 manufacturer's certificate of analysis for lot number SE240163. For global proteome analysis,  
629 protein-centric data, including TMT intensity values divided by the corresponding replicate  
630 control, were summarized in a table, which was further filtered to remove non-mouse  
631 contaminants and proteins with less than 2 unique peptides. For phosphoproteome analysis,  
632 peptide-centric data, including TMT intensity values divided by the corresponding replicate  
633 control, were summarized and filtered to remove non-mouse peptides.

634

### 635 **Immunoprecipitation and Western Blotting**

636 Shank3 protein was enriched by immunoprecipitation before analysis by western  
637 blotting. At the end of scaling induction, neurons were lysed in RIPA buffer (150 mM NaCl, 50  
638 mM Tris, 1% Triton X-100, 0.1% SDS, 0.5% sodium deoxycholate, 1 mM EDTA) containing  
639 cocktails of protease inhibitors (cOmplete, Sigma-Aldrich) and phosphatase inhibitors

640 (PhosSTOP, Sigma-Aldrich), incubated on a rotating rocker at 4°C for 20 minutes, and  
641 centrifuged at 13,000 rpm for 15 minutes. The supernatants were then collected, and the  
642 protein concentration was measured using a commercial BCA assay (Thermo Fisher  
643 Scientific). To enrich the Shank3 protein, cell lysates (~800 ng) were incubated with guinea pig  
644 anti-Shank3 antibodies (1 µg, 162304, Synaptic Systems) on the rotating rocker at 4°C  
645 overnight. On the next day, the protein-antibody mixtures were incubated with magnetic  
646 protein-G beads (20 µl, Thermo Fisher Scientific) for another hour. After being washed  
647 thoroughly with RIPA buffer, the protein-antibody-bead mixtures were resuspended directly in  
648 the SDS-containing loading buffer (30 µl, LI-COR) and the Shank3 proteins were eluted into  
649 the buffer by heating at 70°C for 10 minutes. Once cooled down on the ice, the eluates were  
650 loaded into the 7% NuPAGE tris-acetate gel (Thermo Fisher Scientific), electrophoresed until  
651 well separated, and then slowly transferred to a PVDF membrane at 4°C overnight. Afterward,  
652 the membranes were incubated with the Odyssey blocking buffer (LI-COR) at room  
653 temperature for one hour and probed for Shank3 phosphorylation with a rabbit anti-pS1615  
654 antibody (1:1000, Broad Institute) at 4°C overnight, followed by one-hour incubation with the  
655 donkey anti-rabbit IRDye 680RD antibody (1:5000, LI-COR) at room temperature. After  
656 thorough washes, the membranes were imaged on a GelDoc imager (Bio-Rad). To measure  
657 total Shank3, the membranes were subject to a second round of staining where the guinea pig  
658 anti-Shank3 antibody (1:1000) and a donkey anti-guinea pig IRDye 800CW antibody were  
659 used. All the bands were visualized and quantified using the Image Lab Software (Bio-Rad).  
660 Data were collected from at least four independent experiments, in which all conditions were  
661 run in parallel with and normalized to the untreated control.

662



663 **Quantitative Liquid Chromatography-Tandem Mass Spectrometry (LC-MS/MS) Analysis**  
664 **of Rat Shank3 Phosphorylation**

665 **Sample preparation:** The immunoprecipitation method described above was used to  
666 extract the Shank3 protein for mass spectrometry with the following modifications: neurons  
667 from two 10-cm plates were pooled for each replicate. Two replicates were prepared for each  
668 condition (untreated and TTX-treated) and were subject to the electrophoresis protocol  
669 described above. Once separated, the bands containing Shank3 were visualized on the gel  
670 with the Coomassie Blue SafeStain (Thermo Fisher Scientific), cut out with a clean blade, and  
671 sent to Taplin Mass Spectrometry Facility at Harvard for further processing and analysis.

672 **In-gel digestion:** Excised gel bands were cut into approximately 1 mm<sup>3</sup> pieces. The  
673 samples were reduced with 1 mM dithiothreitol for 30 minutes at 60°C and then alkylated with  
674 5 mM iodoacetamide for 15 minutes in the dark at room temperature. Gel pieces were then  
675 subjected to a modified in-gel trypsin digestion procedure (Shevchenko et al., 1996). Gel  
676 pieces were washed and dehydrated with acetonitrile for 10 min, followed by removal of  
677 acetonitrile. Pieces were then completely dried in a speed-vac. Rehydration of the gel pieces  
678 was with 50 mM ammonium bicarbonate solution containing 12.5 ng/μl modified sequencing-  
679 grade trypsin (Promega, Madison, WI) at 4°C. Samples were then placed in a 37°C room  
680 overnight. Peptides were later extracted by removing the ammonium bicarbonate solution,  
681 followed by one wash with a solution containing 50% acetonitrile and 1% formic acid. The  
682 extracts were then dried in a speed-vac (~1 hr).

683 **TMT labeling:** Samples were re-suspended in 20 μl 200 mM HEPES buffer along with 6  
684 μl of acetonitrile; 2 μl of TMT0 or TMT Super Heavy were added as light and heavy labels to  
685 each set of samples. After one hour 2 μl of a 5% hydroxylamine was added for 15 minutes



686 followed by the addition of 10  $\mu$ l of 20% formic acid. Samples were mixed and then dried.  
687 Desalting of the samples was performed with an in-house de-salting tube using reverse phase  
688 C18 Empore™ SPE Disks (3M, Eagan, MN)

689 **Mass spectrometry analysis:** On the day of analysis, the samples were reconstituted  
690 in 10  $\mu$ l of HPLC solvent A (2.5% acetonitrile, 0.1% formic acid). A nano-scale reverse-phase  
691 HPLC capillary column was created by packing 2.6  $\mu$ m C18 spherical silica beads into a fused  
692 silica capillary (100  $\mu$ m inner diameter x ~30 cm length) with a flame-drawn tip (Peng & Gygi,  
693 2001). After equilibrating the column, each sample was loaded via a Famos auto sampler (LC  
694 Packings, San Francisco CA) onto the column. A gradient was formed and peptides were  
695 eluted with increasing concentrations of solvent B (97.5% acetonitrile, 0.1% formic acid). As  
696 each peptide was eluted, they were subjected to electrospray ionization, and then they entered  
697 into an LTQ Orbitrap Velos Pro ion-trap mass spectrometer (Thermo Fisher Scientific, San  
698 Jose, CA). Eluting peptides were detected, isolated, and fragmented to produce a tandem  
699 mass spectrum of specific fragment ions for each peptide. Peptide sequences (and hence  
700 protein identity) were determined by matching protein or translated nucleotide databases with  
701 the acquired fragmentation pattern by the software program, Sequest (ThermoFinnigan, San  
702 Jose, CA) (Eng et al., 1994). The static modifications of 224.1525 mass units were set for  
703 lysine and the N-terminal of peptides (light label), along with 57.0215 mass units on cysteine  
704 (iodoacetamide). Differential modifications of 11.0243 mass units were set for lysine and the  
705 N-terminal of peptides (heavy label) along with 79.9663 mass units to serine, threonine, and  
706 tyrosine was included in the database searches to determine phosphopeptides.  
707 Phosphorylation assignments were determined by the Ascore algorithm (Beausoleil et al.,

708 2006). All databases include a reversed version of all the sequences and the data were filtered  
709 to between a one and two percent peptide false discovery rate.

710

### 711 **Expression Constructs and Generation of Shank3 Mutants**

712 The construct expressing wild-type rat Shank3 (AJ133120.1) with an N-terminal GFP  
713 tag was obtained from Chiara Verpelli (Verpelli et al., 2011). Constructs expressing GFP-  
714 tagged or HA-tagged Shank3 phospho-mutants were generated using the Gibson Assembly kit  
715 (NEB) with the wild-type Shank3 as the template. For the double phospho-mimetic mutant,  
716 residues 1586 (TCC) and 1615 (AGC) were mutated from serine to aspartic acid (GAC). For  
717 the double phospho-deficient mutant, the same residues were mutated from serine to alanine  
718 (GCA). The coding regions of all constructs were fully sequenced to ensure that no unwanted  
719 random mutations were generated during cloning.

720

### 721 **Generation and Validation of Phosphospecific Shank3 Antibody**

722 Polyclonal antibodies targeting pS1615 Shank3 were generated in rabbits using the  
723 immunogen peptide AARLFS[pS]LGELSTI and purified against the phosphopeptide and  
724 counter selected against the non-phospho peptide using affinity chromatography (21st Century  
725 Biochemicals, Marlborough MA). We then conducted two experiments to validate the  
726 specificity of the antibody. In the first experiment, we transfected HEK293 cells with either HA-  
727 tagged wild-type Shank3 or the S1586A/S1615A mutant, and 48 hours later performed  
728 immunoprecipitation and immunoblotting as described above (Figure 2 – figure supplement  
729 1A). In the second experiment, protein lysates containing wild-type HA-Shank3 were subjected  
730 to the same western blotting protocol except that after being transferred to the PVDF

731 membrane, one set of the replicates were treated with lambda phosphatase (NEB) overnight at  
732 25°C before incubation with the pS1615 antibody (Figure 2 – figure supplement 1B).

733

### 734 **Protein Phosphatase 2A (PP2A) Activity Assay**

735 Dissociated cortical neurons were prepared as described above. After being treated  
736 with TTX for 1 hr or 24 hrs, cells were lysed and sonicated in phosphatase extraction buffer (20  
737 mM imidazole-HCl, 2 mM EDTA, 2 mM EGTA, pH 7.0 with cocktails of protease inhibitors and  
738 phosphatase inhibitors). Untreated sister cultures were prepared in parallel and served as  
739 controls. After centrifugation, protein concentrations of the supernatants were determined  
740 using the BCA assay and diluted to 500 µg/mL per sample. The same amounts of cell lysates  
741 were then subject to a commercial colorimetric PP2A activity assay (Millipore).

742

### 743 **Immunocytochemistry**

744 24 or 48 hours after transfection, neurons were fixed with 4% paraformaldehyde for 15  
745 minutes and subject to the established staining protocol (Gainey et al., 2015; Tatavarty et al.,  
746 2020). To probe endogenous or exogenously expressed Shank3, cells were permeabilized  
747 with the blocking buffer (0.1% Triton X-100/10% goat serum in PBS) at room temperature for  
748 45 minutes. They were then incubated with the dilution buffer (5% goat serum in PBS)  
749 containing the following primary antibodies at 4°C overnight: chicken anti-GFP (1:1000, Aves  
750 Labs), guinea pig anti-Shank3 (1:1000, Synaptic Systems), guinea pig or rabbit anti-VGluT1  
751 (1:1000, Synaptic Systems). To stain surface GluA2, the protocol was modified such that prior  
752 to permeabilization, cells were first incubated with mouse anti-GluA2 (1:1000, gift from Eric  
753 Gouaux, Vollum Institute, Oregon Health & Science University, Portland, Oregon) diluted in the

754 blocking buffer without Triton X-100 for 1 hr at room temperature. On the next day, neurons  
755 were washed three times with PBS and incubated with the dilution buffer containing the  
756 following secondary antibodies at room temperature for one hour: goat anti-chicken Alexa-488,  
757 goat anti-mouse Alexa-555, goat anti-guinea pig Alexa-555, goat anti-guinea pig Alexa-647,  
758 and goat anti-rabbit Alexa-647 (1:400, Thermo Fisher Scientific). After 3 more washes with  
759 PBS, the glass bottoms containing stained neurons were detached from the dishes, mounted  
760 onto the slides using DAPI-Fluoromount-G mounting medium (SouthernBiotech), and sealed  
761 with nail polish.

762

### 763 **Image Acquisition and Analysis**

764 All the images were acquired using a 63X oil immersion objective on a laser-scanning  
765 confocal microscope (LSM880, Zeiss) using ZEN Black acquisition software. For all  
766 experiments, acquisition settings including laser power, gain/offset, and pinhole size were kept  
767 consistent. During image acquisition, pyramidal neurons were identified by their typical  
768 teardrop-shaped somata and apical-like dendrite. For each neuron, ~12 stacked images (step  
769 size: 0.33  $\mu\text{m}$ ) were obtained to include the apical dendrites and their dendritic branches, and  
770 then subject to maximum intensity projection using ZEN Black. To quantify the colocalization of  
771 synaptic proteins and their signal intensities, images were analyzed using the MetaMorph  
772 software (Molecular Devices). In all cases, GFP expression was first thresholded to create a  
773 mask that outlined the neuron. A region of interest was then manually drawn to include the  
774 dendritic branches distal to the primary branch point of apical-like dendrite. A threshold was set  
775 for the signal intensity in each channel to exclude background noise and was kept consistent  
776 across experimental groups. The granularity function in MetaMorph was then used to threshold

777 puncta in each channel (puncta size: 0.5 – 5  $\mu\text{m}$ ). Binary images were generated to outline  
778 identified puncta in each channel, and the colocalized puncta were determined using the  
779 Logical AND operation. A synapse was defined as a punctum double-labeled with GFP and  
780 VGLuT1(Figure 3D, Figure 5, Figure 5 – figure supplement 1) or triple-labeled with GFP,  
781 sGluA2, and VGLuT1 (Figure 7, Figure 6 – figure supplement 2). Total puncta intensity for each  
782 channel at colocalized sites was then measured. The experimental conditions were always run  
783 in parallel with the control condition on sister cultures from the same dissociation, and the total  
784 puncta intensity measured in the experimental conditions was normalized to the mean total  
785 puncta intensity of control in sister cultures unless described otherwise.

786

### 787 **mEPSC Recordings**

788 Recordings were performed in whole-cell voltage clamp at room temperature; holding  
789 potential was -70 mV. Neurons with pyramidal morphology were targeted by visual inspection.  
790 Bath solution was ACSF containing (in mM): 126 NaCl, 5.5 KCl, 2 MgSO<sub>4</sub>, 1 NaH<sub>2</sub>PO<sub>4</sub>, 25  
791 NaHCO<sub>3</sub>, 2 CaCl<sub>2</sub>, 14 dextrose; and 25  $\mu\text{M}$  picrotoxin, 25  $\mu\text{M}$  D-amino-5-phosphovaleric acid  
792 (AP5), and 0.1  $\mu\text{M}$  TTX to isolate AMPA-mediated mEPSCs. Internal solution composition (in  
793 mM) was: 120 KMeSO<sub>4</sub>, 10 KCl, 2 MgSO<sub>4</sub>, 10 K-Hepes, 0.5 EGTA, 3 K<sub>2</sub>ATP, 0.3 NaGTP, and  
794 10 Na<sub>2</sub>phosphocreatine. Dextrose was added to adjust osmolarity to 320-330 mOsm. Neurons  
795 were excluded if resting membrane potential ( $V_m$ ) was  $> -55$  mV, series resistance ( $R_s$ ) was  $>$   
796 20 M $\Omega$ , input resistance ( $R_{in}$ ) was  $< 100$  M $\Omega$ ,  $R_{in}$  or  $V_m$  changed by  $> 30\%$ , or  $< 25$  mEPSCs  
797 were obtained. MEPSCs were detected and analyzed using in-house software (see (Pacheco  
798 et al., 2021); detection criteria included amplitudes  $> 5$  pA and rise times  $< 3$  ms. To construct  
799 cumulative histograms, the first 25 events for each neuron were included.

800

## 801 **Statistical Analysis**

### 802 ***Western blotting, PP2A activity assay, imaging, and electrophysiology***

803 **experiments:** GraphPad Prism software was used to conduct statistical analyses. For each  
804 experiment, data distribution in individual condition was tested for normality using the  
805 Anderson-Darling test. If all experimental conditions passed the normality test, a t-test, paired  
806 t-test, or two-way ANOVA was used where appropriate. If one or more conditions failed the  
807 normality test, a Mann-Whitney test or Kruskal-Wallis test was used as indicated. Significant  
808 Kruskal-Wallis tests were then subject to a Dunn's post-hoc test for multiple comparisons. The  
809 significance levels were marked by asterisks (\*): \*:  $P < 0.05$ ; \*\*:  $P < 0.01$ ; \*\*\*:  $P < 0.001$ ; \*\*\*\*:  $P$   
810  $< 0.0001$ .

811 ***Differential abundance analysis of proteomics data:*** Statistical analysis was  
812 performed in the R environment for statistical computing. Sample log<sub>2</sub> TMT ratios were  
813 median-MAD normalized. Proteins and phosphosites with more than 50% missing values were  
814 removed. In order to identify proteins and phosphopeptides that respond to TTX or BIC  
815 treatment, a linear model with time groups as factors was fitted and a moderated F-test was  
816 performed on all coefficients using the limma package (Ritchie et al., 2015). Multiple  
817 hypothesis testing correction was performed using the BH method. Bidirectionally regulated  
818 phosphosites across TTX and BIC treatment were those that showed significant regulation by  
819 F-test in both treatments, as well as opposite signs when calculating the mean log<sub>2</sub>FC across  
820 all time points for each treatment.

821 ***Pathway enrichment and network visualization:*** Proteins and phosphosites showing  
822 differential abundance in response to TTX or BIC treatment were clustered using the k-means

823 methods (k=4 for BIC and k=3 for TTX). The optimal number of clusters was calculated using  
824 the elbow method using the total within sums of squares. Pathway enrichment analysis was  
825 performed for each cluster with the g:profiler tool (Raudvere et al., 2019). The background list  
826 of proteins was set to all detected in the proteomics analysis, and the databases used for  
827 annotation were Gene Ontology, KEGG, Wikipathways, and Reactome. The list of enriched  
828 pathways and genes contained in each pathway were exported to Cytoscape (Shannon et al.,  
829 2003). The EnrichmentMap app was used to generate a network of enriched pathways with the  
830 following parameters (min pathway p-value = 0.01; overlap index = 1) (Merico et al., 2010).

831 ***Interactive visualization of proteomic, phosphoproteomic data, and derived***  
832 ***pathway activity scores:*** All proteome and phosphoproteome data can be explored as  
833 interactive R Markdown documents at [https://proteomics.broadapps.org/HSP\\_TTX/](https://proteomics.broadapps.org/HSP_TTX/) and  
834 [https://proteomics.broadapps.org/HSP\\_Bic/](https://proteomics.broadapps.org/HSP_Bic/). In addition to TTX/Bic-induced temporal changes  
835 on protein and phosphosite-level, the apps enable the user to explore pathway-level changes  
836 across time points. To project protein and phosphosite expression matrices  
837 onto [MSigDB](#) canonical pathways (c2.cp v7.4) single sample Gene Set Enrichment Analysis  
838 (ssGSEA) was used. TMT ratios of phosphosites and proteins mapping to the same gene  
839 symbol were combined by median expression prior to ssGSEA. The resulting normalized  
840 enrichment scores (NES) can be interpreted as *pathway activity scores* and served as input for  
841 the longitudinal analysis described above.

842

## 843 **ACKNOWLEDGEMENT**

844 We thank Taplin Mass Spectrometry Facility (Harvard) for their assistance in processing  
845 and analyzing the rat MS experiment and Lirong Wang for her technical support. This work

846 was supported by the NIH grants R35 NS111562 (GGT), F32 HL154711 (PMJB), Simons  
847 Foundation Award 345485 (GGT), and Stanley Center for Psychiatric Research (JRC).

848

## 849 **COMPETING INTERESTS**

850 The authors declare no competing interests.

851

## 852 **REFERENCES**

- 853 Baron, M. K., Boeckers, T. M., Vaida, B., Faham, S., Gingery, M., Sawaya, M. R., Salyer, D.,  
854 Gundelfinger, E. D., & Bowie, J. U. (2006). An Architectural Framework That May Lie at  
855 the Core of the Postsynaptic Density. *Science*, *311*(5760), 531–535.  
856 <https://doi.org/10.1126/science.1118995>
- 857 Beausoleil, S. A., Villén, J., Gerber, S. A., Rush, J., & Gygi, S. P. (2006). A probability-based  
858 approach for high-throughput protein phosphorylation analysis and site localization.  
859 *Nature Biotechnology*, *24*(10), 1285–1292. <https://doi.org/10.1038/nbt1240>
- 860 Betancur, C., & Buxbaum, J. D. (2013). SHANK3 haploinsufficiency: A “common” but  
861 underdiagnosed highly penetrant monogenic cause of autism spectrum disorders.  
862 *Molecular Autism*, *4*(1), 17. <https://doi.org/10.1186/2040-2392-4-17>
- 863 Bialojan, C., & Takai, A. (1988). Inhibitory effect of a marine-sponge toxin, okadaic acid, on  
864 protein phosphatases. Specificity and kinetics. *Biochemical Journal*, *256*(1), 283–290.  
865 <https://doi.org/10.1042/bj2560283>
- 866 Boeckers, T. M., Liedtke, T., Spilker, C., Dresbach, T., Bockmann, J., Kreutz, M. R., &  
867 Gundelfinger, E. D. (2005). C-terminal synaptic targeting elements for postsynaptic



- 868 density proteins ProSAP1/Shank2 and ProSAP2/Shank3. *Journal of Neurochemistry*,  
869 92(3), 519–524. <https://doi.org/10.1111/j.1471-4159.2004.02910.x>
- 870 Cohen, P., Klumpp, S., & Schelling, D. L. (1989). An improved procedure for identifying and  
871 quantitating protein phosphatases in mammalian tissues. *FEBS Letters*, 250(2), 596–  
872 600. [https://doi.org/10.1016/0014-5793\(89\)80803-8](https://doi.org/10.1016/0014-5793(89)80803-8)
- 873 Colbran, R. J. (2004). Protein Phosphatases and Calcium/Calmodulin-Dependent Protein  
874 Kinase II-Dependent Synaptic Plasticity. *Journal of Neuroscience*, 24(39), 8404–8409.  
875 <https://doi.org/10.1523/JNEUROSCI.3602-04.2004>
- 876 Desch, K., Langer, J. D., & Schuman, E. M. (2021). Dynamic bi-directional phosphorylation  
877 events associated with the reciprocal regulation of synapses during homeostatic up-  
878 and down-scaling. *Cell Reports*, 36(8), 109583.  
879 <https://doi.org/10.1016/j.celrep.2021.109583>
- 880 Diering, G. H., & Huganir, R. L. (2018). The AMPA Receptor Code of Synaptic Plasticity.  
881 *Neuron*, 100(2), 314–329. <https://doi.org/10.1016/j.neuron.2018.10.018>
- 882 Dörrbaum, A. R., Alvarez-Castelao, B., Nassim-Assir, B., Langer, J. D., & Schuman, E. M.  
883 (2020). Proteome dynamics during homeostatic scaling in cultured neurons. *ELife*, 9,  
884 e52939. <https://doi.org/10.7554/eLife.52939>
- 885 Dosemeci, A., & Jaffe, H. (2010). Regulation of phosphorylation at the postsynaptic density  
886 during different activity states of Ca<sup>2+</sup>/calmodulin-dependent protein kinase II.  
887 *Biochemical and Biophysical Research Communications*, 391(1), 78–84.  
888 <https://doi.org/10.1016/j.bbrc.2009.10.167>
- 889 duBell, W. H., Gigena, M. S., Guatimosim, S., Long, X., Lederer, W. J., & Rogers, T. B. (2002).  
890 Effects of PP1/PP2A inhibitor calyculin A on the E-C coupling cascade in murine

891 ventricular myocytes. *American Journal of Physiology-Heart and Circulatory Physiology*,  
892 282(1), H38–H48. <https://doi.org/10.1152/ajpheart.00536.2001>

893 Eng, J. K., McCormack, A. L., & Yates, J. R. (1994). An approach to correlate tandem mass  
894 spectral data of peptides with amino acid sequences in a protein database. *Journal of*  
895 *the American Society for Mass Spectrometry*, 5(11), 976–989.  
896 [https://doi.org/10.1016/1044-0305\(94\)80016-2](https://doi.org/10.1016/1044-0305(94)80016-2)

897 Fernandes, D., & Carvalho, A. L. (2016). Mechanisms of homeostatic plasticity in the excitatory  
898 synapse. *Journal of Neurochemistry*, 139(6), 973–996. <https://doi.org/10.1111/jnc.13687>

899 Gaaney, M. A., Tatavarty, V., Nahmani, M., Lin, H., & Turrigiano, G. G. (2015). Activity-  
900 dependent synaptic GRIP1 accumulation drives synaptic scaling up in response to  
901 action potential blockade. *Proceedings of the National Academy of Sciences of the*  
902 *United States of America*, 112(27), E3590-3599.  
903 <https://doi.org/10.1073/pnas.1510754112>

904 Goujon, M., McWilliam, H., Li, W., Valentin, F., Squizzato, S., Paern, J., & Lopez, R. (2010). A  
905 new bioinformatics analysis tools framework at EMBL–EBI. *Nucleic Acids Research*,  
906 38(suppl\_2), W695–W699. <https://doi.org/10.1093/nar/gkq313>

907 Grabrucker, A. M., Schmeisser, M. J., Schoen, M., & Boeckers, T. M. (2011). Postsynaptic  
908 ProSAP/Shank scaffolds in the cross-hair of synaptopathies. *Trends in Cell Biology*,  
909 21(10), 594–603. <https://doi.org/10.1016/j.tcb.2011.07.003>

910 Guan, J.-S., Su, S. C., Gao, J., Joseph, N., Xie, Z., Zhou, Y., Durak, O., Zhang, L., Zhu, J. J.,  
911 Clauser, K. R., Carr, S. A., & Tsai, L.-H. (2011). Cdk5 Is Required for Memory Function  
912 and Hippocampal Plasticity via the cAMP Signaling Pathway. *PLOS ONE*, 6(9), e25735.  
913 <https://doi.org/10.1371/journal.pone.0025735>

- 914 Hayashi, M. K., Tang, C., Verpelli, C., Narayanan, R., Stearns, M. H., Xu, R.-M., Li, H., Sala,  
915 C., & Hayashi, Y. (2009). The Postsynaptic Density Proteins Homer and Shank Form a  
916 Polymeric Network Structure. *Cell*, *137*(1), 159–171.  
917 <https://doi.org/10.1016/j.cell.2009.01.050>
- 918 Hu, J.-H., Park, J. M., Park, S., Xiao, B., Dehoff, M. H., Kim, S., Hayashi, T., Schwarz, M. K.,  
919 Huganir, R. L., Seeburg, P. H., Linden, D. J., & Worley, P. F. (2010). Homeostatic  
920 Scaling Requires Group I mGluR Activation Mediated by Homer1a. *Neuron*, *68*(6),  
921 1128–1142. <https://doi.org/10.1016/j.neuron.2010.11.008>
- 922 Hwang, H., Szucs, M. J., Ding, L. J., Allen, A., Ren, X., Haensgen, H., Gao, F., Rhim, H.,  
923 Andrade, A., Pan, J. Q., Carr, S. A., Ahmad, R., & Xu, W. (2021). Neurogranin,  
924 Encoded by the Schizophrenia Risk Gene NRG1, Bidirectionally Modulates Synaptic  
925 Plasticity via Calmodulin-Dependent Regulation of the Neuronal Phosphoproteome.  
926 *Biological Psychiatry*, *89*(3), 256–269. <https://doi.org/10.1016/j.biopsych.2020.07.014>
- 927 Ibata, K., Sun, Q., & Turrigiano, G. G. (2008). Rapid synaptic scaling induced by changes in  
928 postsynaptic firing. *Neuron*, *57*(6), 819–826.  
929 <https://doi.org/10.1016/j.neuron.2008.02.031>
- 930 Ishihara, H., Martin, B. L., Brautigan, D. L., Karaki, H., Ozaki, H., Kato, Y., Fusetani, N.,  
931 Watabe, S., Hashimoto, K., Uemura, D., & Hartshorne, D. J. (1989). Calyculin A and  
932 okadaic acid: Inhibitors of protein phosphatase activity. *Biochemical and Biophysical  
933 Research Communications*, *159*(3), 871–877. [https://doi.org/10.1016/0006-  
934 291X\(89\)92189-X](https://doi.org/10.1016/0006-291X(89)92189-X)
- 935 Jeong, J., Li, Y., & Roche, K. W. (2021). CaMKII Phosphorylation Regulates Synaptic  
936 Enrichment of Shank3. *ENeuro*, *8*(3). <https://doi.org/10.1523/ENEURO.0481-20.2021>

- 937 Jiang, Y., & Ehlers, M. D. (2013). Modeling Autism by SHANK Gene Mutations in Mice.  
938 *Neuron*, 78(1), 8–27. <https://doi.org/10.1016/j.neuron.2013.03.016>
- 939 Kavalali, E. T., & Monteggia, L. M. (2020). Targeting Homeostatic Synaptic Plasticity for  
940 Treatment of Mood Disorders. *Neuron*, 106(5), 715–726.  
941 <https://doi.org/10.1016/j.neuron.2020.05.015>
- 942 Launey, T., Endo, S., Sakai, R., Harano, J., & Ito, M. (2004). Protein phosphatase 2A inhibition  
943 induces cerebellar long-term depression and declustering of synaptic AMPA receptor.  
944 *Proceedings of the National Academy of Sciences*, 101(2), 676–681.  
945 <https://doi.org/10.1073/pnas.0302914101>
- 946 Li, J., Wilkinson, B., Clementel, V. A., Hou, J., O'Dell, T. J., & Coba, M. P. (2016). Long-term  
947 potentiation modulates synaptic phosphorylation networks and reshapes the structure of  
948 the postsynaptic interactome. *Science Signaling*, 9(440), rs8–rs8.  
949 <https://doi.org/10.1126/scisignal.aaf6716>
- 950 Louros, S. R., Caldeira, G. L., & Carvalho, A. L. (2018). Stargazin Dephosphorylation Mediates  
951 Homeostatic Synaptic Downscaling of Excitatory Synapses. *Frontiers in Molecular  
952 Neuroscience*, 0. <https://doi.org/10.3389/fnmol.2018.00328>
- 953 Mao, W., Salzberg, A. C., Uchigashima, M., Hasegawa, Y., Hock, H., Watanabe, M., Akbarian,  
954 S., Kawasawa, Y. I., & Futai, K. (2018). Activity-Induced Regulation of Synaptic  
955 Strength through the Chromatin Reader L3mbtl1. *Cell Reports*, 23(11), 3209–3222.  
956 <https://doi.org/10.1016/j.celrep.2018.05.028>
- 957 Mauna, J. C., Miyamae, T., Pulli, B., & Thiels, E. (2011). Protein phosphatases 1 and 2A are  
958 both required for long-term depression and associated dephosphorylation of cAMP

- 959 response element binding protein in hippocampal area CA1 in vivo. *Hippocampus*,  
960 21(10), 1093–1104. <https://doi.org/10.1002/hipo.20823>
- 961 McWilliam, H., Li, W., Uludag, M., Squizzato, S., Park, Y. M., Buso, N., Cowley, A. P., &  
962 Lopez, R. (2013). Analysis Tool Web Services from the EMBL-EBI. *Nucleic Acids*  
963 *Research*, 41(W1), W597–W600. <https://doi.org/10.1093/nar/gkt376>
- 964 Merico, D., Isserlin, R., Stueker, O., Emili, A., & Bader, G. D. (2010). Enrichment map: A  
965 network-based method for gene-set enrichment visualization and interpretation. *PLoS*  
966 *ONE*, 5(11). <https://doi.org/10.1371/journal.pone.0013984>
- 967 Mertins, P., Tang, L. C., Krug, K., Clark, D. J., Gritsenko, M. A., Chen, L., Clauser, K. R.,  
968 Clauss, T. R., Shah, P., Gillette, M. A., Petyuk, V. A., Thomas, S. N., Mani, D. R.,  
969 Mundt, F., Moore, R. J., Hu, Y., Zhao, R., Schnaubelt, M., Keshishian, H., ... Carr, S. A.  
970 (2018). Reproducible workflow for multiplexed deep-scale proteome and  
971 phosphoproteome analysis of tumor tissues by liquid chromatography-mass  
972 spectrometry. *Nature Protocols*, 13(7), 1632–1661. [https://doi.org/10.1038/s41596-018-](https://doi.org/10.1038/s41596-018-0006-9)  
973 0006-9
- 974 Mitsuhashi, S., Matsuura, N., Ubukata, M., Oikawa, H., Shima, H., & Kikuchi, K. (2001).  
975 Tautomycetin Is a Novel and Specific Inhibitor of Serine/Threonine Protein Phosphatase  
976 Type 1, PP1. *Biochemical and Biophysical Research Communications*, 287(2), 328–  
977 331. <https://doi.org/10.1006/bbrc.2001.5596>
- 978 Naisbitt, S., Kim, E., Tu, J. C., Xiao, B., Sala, C., Valtschanoff, J., Weinberg, R. J., Worley, P.  
979 F., & Sheng, M. (1999). Shank, a Novel Family of Postsynaptic Density Proteins that  
980 Binds to the NMDA Receptor/PSD-95/GKAP Complex and Cortactin. *Neuron*, 23(3),  
981 569–582. [https://doi.org/10.1016/S0896-6273\(00\)80809-0](https://doi.org/10.1016/S0896-6273(00)80809-0)

- 982 Pacheco, A. T., Bottorff, J., Gao, Y., & Turrigiano, G. G. (2021). Sleep Promotes Downward  
983 Firing Rate Homeostasis. *Neuron*, *109*(3), 530-544.e6.  
984 <https://doi.org/10.1016/j.neuron.2020.11.001>
- 985 Peng, J., & Gygi, S. P. (2001). Proteomics: The move to mixtures. *Journal of Mass*  
986 *Spectrometry*, *36*(10), 1083–1091. <https://doi.org/10.1002/jms.229>
- 987 Perfitt, T. L., Stauffer, P. E., Spiess, K. L., & Colbran, R. J. (2020). CaMKII $\alpha$  phosphorylation of  
988 Shank3 modulates ABI1-Shank3 interaction. *Biochemical and Biophysical Research*  
989 *Communications*, *524*(1), 262–267. <https://doi.org/10.1016/j.bbrc.2020.01.089>
- 990 Pribiag, H., & Stellwagen, D. (2013). TNF- $\alpha$  Downregulates Inhibitory Neurotransmission  
991 through Protein Phosphatase 1-Dependent Trafficking of GABAA Receptors. *Journal of*  
992 *Neuroscience*, *33*(40), 15879–15893. [https://doi.org/10.1523/JNEUROSCI.0530-](https://doi.org/10.1523/JNEUROSCI.0530-13.2013)  
993 [13.2013](https://doi.org/10.1523/JNEUROSCI.0530-13.2013)
- 994 Raudvere, U., Kolberg, L., Kuzmin, I., Arak, T., Adler, P., Peterson, H., & Vilo, J. (2019).  
995 G:Profiler: A web server for functional enrichment analysis and conversions of gene lists  
996 (2019 update). *Nucleic Acids Research*, *47*(W1), W191–W198.  
997 <https://doi.org/10.1093/nar/gkz369>
- 998 Ritchie, M. E., Phipson, B., Wu, D., Hu, Y., Law, C. W., Shi, W., & Smyth, G. K. (2015). Limma  
999 powers differential expression analyses for RNA-sequencing and microarray studies.  
1000 *Nucleic Acids Research*, *43*(7), e47. <https://doi.org/10.1093/nar/gkv007>
- 1001 Schanzenbächer, C. T., Langer, J. D., & Schuman, E. M. (2018). Time- and polarity-dependent  
1002 proteomic changes associated with homeostatic scaling at central synapses. *ELife*, *7*,  
1003 e33322. <https://doi.org/10.7554/eLife.33322>

- 1004 Schanzenbächer, C. T., Sambandan, S., Langer, J. D., & Schuman, E. M. (2016). Nascent  
1005 Proteome Remodeling following Homeostatic Scaling at Hippocampal Synapses.  
1006 *Neuron*, *92*(2), 358–371. <https://doi.org/10.1016/j.neuron.2016.09.058>
- 1007 Schaukowitch, K., Reese, A. L., Kim, S.-K., Kilaru, G., Joo, J.-Y., Kavalali, E. T., & Kim, T.-K.  
1008 (2017). An Intrinsic Transcriptional Program Underlying Synaptic Scaling during Activity  
1009 Suppression. *Cell Reports*, *18*(6), 1512–1526.  
1010 <https://doi.org/10.1016/j.celrep.2017.01.033>
- 1011 Shadforth, I. P., Dunkley, T. P., Lilley, K. S., & Bessant, C. (2005). i-Tracker: For quantitative  
1012 proteomics using iTRAQ™. *BMC Genomics*, *6*(1), 145. [https://doi.org/10.1186/1471-](https://doi.org/10.1186/1471-2164-6-145)  
1013 [2164-6-145](https://doi.org/10.1186/1471-2164-6-145)
- 1014 Shannon, P., Markiel, A., Ozier, O., Baliga, N. S., Wang, J. T., Ramage, D., Amin, N.,  
1015 Schwikowski, B., & Ideker, T. (2003). Cytoscape: A Software Environment for Integrated  
1016 Models. *Genome Research*, *13*(11), 2498–2504.  
1017 <https://doi.org/10.1101/gr.1239303.metabolite>
- 1018 Shevchenko, A., Wilm, M., Vorm, O., & Mann, M. (1996). Mass spectrometric sequencing of  
1019 proteins silver-stained polyacrylamide gels. *Analytical Chemistry*, *68*(5), 850–858.  
1020 <https://doi.org/10.1021/ac950914h>
- 1021 Shin, S. M., Zhang, N., Hansen, J., Gerges, N. Z., Pak, D. T. S., Sheng, M., & Lee, S. H.  
1022 (2012). GKAP orchestrates activity-dependent postsynaptic protein remodeling and  
1023 homeostatic scaling. *Nature Neuroscience*, *15*(12), 1655–1666.  
1024 <https://doi.org/10.1038/nn.3259>
- 1025 Sievers, F., Wilm, A., Dineen, D., Gibson, T. J., Karplus, K., Li, W., Lopez, R., McWilliam, H.,  
1026 Remmert, M., Söding, J., Thompson, J. D., & Higgins, D. G. (2011). Fast, scalable



- 1027 generation of high-quality protein multiple sequence alignments using Clustal Omega.  
1028 *Molecular Systems Biology*, 7, 539. <https://doi.org/10.1038/msb.2011.75>
- 1029 Steinmetz, C. C., Tatavarty, V., Sugino, K., Shima, Y., Joseph, A., Lin, H., Rutlin, M., Lambo,  
1030 M., Hempel, C. M., Okaty, B. W., Paradis, S., Nelson, S. B., & Turrigiano, G. G. (2016).  
1031 Upregulation of  $\mu$ 3A Drives Homeostatic Plasticity by Rerouting AMPAR into the  
1032 Recycling Endosomal Pathway. *Cell Reports*, 16(10), 2711–2722.  
1033 <https://doi.org/10.1016/j.celrep.2016.08.009>
- 1034 Stellwagen, D., & Malenka, R. C. (2006). Synaptic scaling mediated by glial TNF- $\alpha$ . *Nature*,  
1035 440(7087), 1054–1059. <https://doi.org/10.1038/nature04671>
- 1036 Sun, Q., & Turrigiano, G. G. (2011). PSD-95 and PSD-93 Play Critical But Distinct Roles in  
1037 Synaptic Scaling Up and Down. *The Journal of Neuroscience*, 31(18), 6800–6808.  
1038 <https://doi.org/10.1523/JNEUROSCI.5616-10.2011>
- 1039 Tan, H. L., Queenan, B. N., & Huganir, R. L. (2015). GRIP1 is required for homeostatic  
1040 regulation of AMPAR trafficking. *Proceedings of the National Academy of Sciences*,  
1041 112(32), 10026–10031. <https://doi.org/10.1073/pnas.1512786112>
- 1042 Tatavarty, V., Pacheco, A. T., Kuhnle, C. G., Lin, H., Koundinya, P., Miska, N. J., Hengen, K.  
1043 B., Wagner, F. F., Hooser, S. D. V., & Turrigiano, G. G. (2020). Autism-Associated  
1044 Shank3 Is Essential for Homeostatic Compensation in Rodent V1. *Neuron*, 106(5), 769-  
1045 777.e4. <https://doi.org/10.1016/j.neuron.2020.02.033>
- 1046 Tatavarty, V., Sun, Q., & Turrigiano, G. G. (2013). How to Scale Down Postsynaptic Strength.  
1047 *Journal of Neuroscience*, 33(32), 13179–13189.  
1048 <https://doi.org/10.1523/JNEUROSCI.1676-13.2013>

- 1049 Thomas, G. M., Rumbaugh, G. R., Harrar, D. B., & Huganir, R. L. (2005). Ribosomal S6 kinase  
1050 2 interacts with and phosphorylates PDZ domain-containing proteins and regulates  
1051 AMPA receptor transmission. *Proceedings of the National Academy of Sciences*,  
1052 102(42), 15006–15011. <https://doi.org/10.1073/pnas.0507476102>
- 1053 Turrigiano, G. (2011). Too Many Cooks? Intrinsic and Synaptic Homeostatic Mechanisms in  
1054 Cortical Circuit Refinement. *Annual Review of Neuroscience*, 34(1), 89–103.  
1055 <https://doi.org/10.1146/annurev-neuro-060909-153238>
- 1056 Turrigiano, G. G. (2008). The self-tuning neuron: Synaptic scaling of excitatory synapses. *Cell*,  
1057 135(3), 422–435. <https://doi.org/10.1016/j.cell.2008.10.008>
- 1058 Turrigiano, G. G., Leslie, K. R., Desai, N. S., Rutherford, L. C., & Nelson, S. B. (1998). Activity-  
1059 dependent scaling of quantal amplitude in neocortical neurons. *Nature*, 391(6670), 892–  
1060 896. <https://doi.org/10.1038/36103>
- 1061 Turrigiano, G. G., & Nelson, S. B. (2004). Homeostatic plasticity in the developing nervous  
1062 system. *Nature Reviews. Neuroscience*, 5(2), 97–107. <https://doi.org/10.1038/nrn1327>
- 1063 Venkatesan, S., Subramaniam, S., Rajeev, P., Chopra, Y., Jose, M., & Nair, D. (2020).  
1064 Differential Scaling of Synaptic Molecules within Functional Zones of an Excitatory  
1065 Synapse during Homeostatic Plasticity. *ENeuro*, 7(2).  
1066 <https://doi.org/10.1523/ENEURO.0407-19.2020>
- 1067 Verpelli, C., Dvoretzkova, E., Vicidomini, C., Rossi, F., Chiappalone, M., Schoen, M., Stefano,  
1068 B. D., Mantegazza, R., Broccoli, V., Böckers, T. M., Dityatev, A., & Sala, C. (2011).  
1069 Importance of Shank3 Protein in Regulating Metabotropic Glutamate Receptor 5  
1070 (mGluR5) Expression and Signaling at Synapses \*. *Journal of Biological Chemistry*,  
1071 286(40), 34839–34850. <https://doi.org/10.1074/jbc.M111.258384>

- 1072 Walsh, A. H., Cheng, A., & Honkanen, R. E. (1997). Fostriecin, an antitumor antibiotic with  
1073 inhibitory activity against serine/threonine protein phosphatases types 1 (PP1) and 2A  
1074 (PP2A), is highly selective for PP2A. *FEBS Letters*, 416(3), 230–234.  
1075 [https://doi.org/10.1016/S0014-5793\(97\)01210-6](https://doi.org/10.1016/S0014-5793(97)01210-6)
- 1076 Wang, L., Adamski, C. J., Bondar, V. V., Craigen, E., Collette, J. R., Pang, K., Han, K., Jain,  
1077 A., Y. Jung, S., Liu, Z., Sifers, R. N., Holder, J. L., & Zoghbi, H. Y. (2020). A kinome-  
1078 wide RNAi screen identifies ERK2 as a druggable regulator of Shank3 stability.  
1079 *Molecular Psychiatry*, 25(10), 2504–2516. <https://doi.org/10.1038/s41380-018-0325-9>
- 1080 Wang, L., Pang, K., Han, K., Adamski, C. J., Wang, W., He, L., Lai, J. K., Bondar, V. V.,  
1081 Duman, J. G., Richman, R., Tolias, K. F., Barth, P., Palzkill, T., Liu, Z., Holder, J. L., &  
1082 Zoghbi, H. Y. (2020). An autism-linked missense mutation in SHANK3 reveals the  
1083 modularity of Shank3 function. *Molecular Psychiatry*, 25(10), 2534–2555.  
1084 <https://doi.org/10.1038/s41380-018-0324-x>
- 1085 Wang, Q., Chiu, S.-L., Koropouli, E., Hong, I., Mitchell, S., Easwaran, T. P., Hamilton, N. R.,  
1086 Gustina, A. S., Zhu, Q., Ginty, D. D., Hugarir, R. L., & Kolodkin, A. L. (2017).  
1087 Neuropilin-2/PlexinA3 Receptors Associate with GluA1 and Mediate Sema3F-  
1088 Dependent Homeostatic Scaling in Cortical Neurons. *Neuron*, 96(5), 1084-1098.e7.  
1089 <https://doi.org/10.1016/j.neuron.2017.10.029>
- 1090 Winder, D. G., & Sweatt, J. D. (2001). Roles of serine/threonine phosphatases in hippocampal  
1091 synaptic plasticity. *Nature Reviews Neuroscience*, 2(7), 461–474.  
1092 <https://doi.org/10.1038/35081514>

- 1093 Woolfrey, K. M., & Dell'Acqua, M. L. (2015). Coordination of Protein Phosphorylation and  
1094 Dephosphorylation in Synaptic Plasticity \*. *Journal of Biological Chemistry*, 290(48),  
1095 28604–28612. <https://doi.org/10.1074/jbc.R115.657262>
- 1096 Yong, A. J. H., Tan, H. L., Zhu, Q., Bygrave, A. M., Johnson, R. C., & Huganir, R. L. (2020).  
1097 Tyrosine phosphorylation of the AMPA receptor subunit GluA2 gates homeostatic  
1098 synaptic plasticity. *Proceedings of the National Academy of Sciences of the United*  
1099 *States of America*, 117(9), 4948–4958. <https://doi.org/10.1073/pnas.1918436117>
- 1100 Zecha, J., Satpathy, S., Kanashova, T., Avanesian, S. C., Kane, M. H., Clauser, K. R.,  
1101 Mertins, P., Carr, S. A., & Kuster, B. (2019). TMT Labeling for the Masses: A Robust  
1102 and Cost-efficient, In-solution Labeling Approach. *Molecular & Cellular Proteomics*,  
1103 18(7), 1468–1478. <https://doi.org/10.1074/MCP.TIR119.001385>

1104

1105

## 1106 **FIGURE LEGENDS**

### 1107 **Figure 1. The temporal phosphoproteome response induced by synaptic scaling**

1108 **protocols.** (A) Heatmap showing the abundance (log<sub>2</sub> TMT ratios to control) of phosphosites  
1109 with a significant response to TTX treatment (F-test, adj. p < 0.1). Hierarchical clustering  
1110 shows three major clusters with different temporal profiles. The number of significant  
1111 phosphosites in each cluster is indicated. (B) Heatmap showing the abundance (log<sub>2</sub> TMT  
1112 ratios to control) of phosphosites with a significant response to BIC treatment (F-test, adj. p <  
1113 0.1). Hierarchical clustering shows four major clusters with different temporal profiles. The  
1114 number of significant phosphosites in each cluster is indicated. (C) Network representation of  
1115 pathway enrichment results from phosphosites showing a significant response to TTX or BIC

1116 treatment. (Top) Temporal profiles are shown for the 3 TTX clusters and 4 BIC clusters; thin  
1117 lines represent individual phosphosites, while thick lines represent the cluster mean. (Bottom)  
1118 Network showing pathways significantly enriched in each of the TTX/BIC clusters. Pathways  
1119 are shown as nodes with colors of each node indicating the associated cluster or clusters.  
1120 Edges connecting the nodes indicate a significant gene overlap between pathways (Jaccard  
1121 Index > 0.5). Related pathways are clustered and the overall function is summarized in text.  
1122 The Synaptic Signaling, Neurogenesis, Cell Membrane, Neuronal Cell Body, and Synapse  
1123 Organization clusters show enrichment in response to TTX and BIC treatment in both  
1124 upregulate and downregulated phosphosites. (D) Upset plot showing the number of unique  
1125 and overlapping regulated phosphosites across BIC and TTX datasets with directionality.  
1126 Groups highlighted in red represent a total of 424 phosphosites showing regulation in both BIC  
1127 and TTX datasets, with opposite directionality. (E) Temporal profile of mouse Shank3 S1539  
1128 phosphosite abundance in response to TTX (left) and BIC (right), displaying opposite response  
1129 to these treatments; different colors represent two biological replicates.

1130

1131 **Figure 2. Neuronal activity bidirectionally modulates the phosphorylation state of**

1132 **Shank3.** (A) The experiment protocol for extraction of Shank3 from rat cultured neocortical  
1133 neurons for further quantitative mass spectrometry (MS) or western blot analyses. (B) Volcano  
1134 plot of quantitative MS data showing Shank3 residues that were differentially phosphorylated in  
1135 TTX-treated samples compared to untreated controls. The log<sub>2</sub> values of fold changes, if  
1136 below zero, indicated hypophosphorylation (paired t test: S1586, adjusted p = 0.034142,  
1137 S1614/5, 0.014444). (C) Top: diagram showing the location of S1586 and S1615 within the rat  
1138 Shank3 protein. Functional domains: ANK = ankyrin repeat; SH3 = SRC homology 3; PDZ =

1139 PSD-95/Disc Large/ZO-1; Pro-rich = proline-rich; SAM = sterile alpha motif. Bottom: homology  
1140 comparison of sequences flanking rat S1586 and S1615 (matching mouse S1539) across  
1141 species (human Shank3: NP\_001358973.1; rat Shank3: NP\_067708.2; mouse Shank3:  
1142 UniprotKB: Q4ACU6.3). Phosphosites of interest are labeled in red; the only residue not  
1143 conserved is shown in blue. (D, E) Representative western blot using an antibody specific for  
1144 phosphorylated S1615, showing changes in Shank3 phosphorylation after 10-min (D) or 24-hr  
1145 (E) treatment with TTX or PTX. (F) Quantification of the fold-change of Shank3 S1615  
1146 phosphorylation in (D). Dashed line indicated the baseline untreated control (one-sample t test:  
1147 TTX,  $p = 0.0005$  (\*\*\*) , PTX,  $p = 0.0675$ ,  $n = 5$  and 5 biological replicates, respectively). (G)  
1148 Quantification of the fold-change of Shank3 S1615 phosphorylation in (E) (one-sample t test:  
1149 TTX,  $p < 0.0001$  (\*\*\*\*) , PTX,  $p = 0.6336$ ,  $n = 7$  and 7 biological replicates, respectively). Solid  
1150 colored horizontal lines indicate the mean, and error bars represent S.E.M.

1151

1152 **Figure 3. Phosphorylation state modulates activity-dependent changes in the synaptic**  
1153 **enrichment of Shank3.** (A) Representative images of synaptic puncta colocalized with  
1154 surface GluA2 (sGluA2) and Shank3 in neuron dendrites  $\pm$  TTX (scale bar = 5  $\mu$ m). (B)  
1155 Quantification of synaptic sGluA2 intensity changes induced by scaling up and down protocols  
1156 (number of neurons: untreated,  $n = 77$ , TTX,  $n = 40$ , PTX,  $n = 29$ ; Kruskal-Wallis test with post-  
1157 hoc Dunn's multiple comparison tests: Un vs. TTX,  $p = 0.0034$  (\*\*), Un vs. PTX,  $p = 0.0408$  (\*),  
1158 TTX vs. PTX,  $p < 0.0001$  (\*\*\*\*)). (C) Quantification of synaptic Shank3 intensity during scaling  
1159 up and down protocols (Kruskal-Wallis test with post-hoc Dunn's tests: Un vs. TTX,  $p = 0.0155$   
1160 (\*), Un vs. PTX,  $p = 0.0205$  (\*), TTX vs. PTX,  $p < 0.0001$  (\*\*\*\*)). (D) Representative images of  
1161 synaptic localization of wild-type Shank3 and Shank3 phospho-mutants (scale bar = 5  $\mu$ m). (E)

1162 Quantification of synaptic intensity of Shank3 phospho-mutants (number of neurons: WT, n =  
1163 33, AA, n = 30, DD, n = 24; Kruskal-Wallis test with post-hoc Dunn's tests: WT vs. AA,  $p >$   
1164 0.9999, WT vs. DD,  $p = 0.0395$  (\*), AA vs. DD,  $p = 0.0039$  (\*\*)). (F) Quantification of the  
1165 density of synaptic puncta containing Shank3 phospho-mutants (number of neurons: WT, n =  
1166 32, AA, n = 30, DD, n = 24; Kruskal-Wallis test:  $p = 0.2814$ ). For imaging experiments here and  
1167 below, each data point represents a single pyramidal neuron, and data were collected from at  
1168 least four independent experiments.

1169

1170 **Figure 4. Increased PP2A activity maintains TTX-induced Shank3 hypophosphorylation.**

1171 (A) Quantification of PP2A activity after 1-hr TTX treatment (Un, n = 5, TTX, n = 5; paired t  
1172 test:  $p = 0.0018$  (\*\*)). (B) Quantification of PP2A activity after 24-hr TTX treatment (Un, n = 7,  
1173 TTX, n = 7; paired t test:  $p = 0.0129$  (\*)). (C, D) Western blot analyses showing changes in  
1174 S1615 phosphorylation after 1-hr (C) or 24-hr (D) TTX treatment, with inhibition of PP2A by  
1175 okadaic acid (OKA, 50 nM) during the last hour of treatment. (E) Quantification of S1615  
1176 phosphorylation in (C) (Two-way ANOVA with post-hoc Tukey's test: Un vs. OKA, 0.1723, Un  
1177 vs. TTX,  $p = 0.0076$  (\*\*), Un vs. TTX/OKA,  $p = 0.0311$  (\*), TTX vs. TTX/OKA,  $p = 0.8942$ , n = 5  
1178 biological replicates). Dashed lines indicated the baseline untreated control. (F) Quantification  
1179 of S1615 phosphorylation in (D). (Two-way ANOVA test with post-hoc Tukey's test: Un vs.  
1180 OKA, = 0.9979, Un vs. TTX,  $p = 0.0503$ , Un vs. TTX/OKA,  $p > 0.9999$ , TTX vs. TTX/OKA,  $p =$   
1181 0.0531, n = 8 biological replicates).

1182

1183 **Figure 5. PP2A activity is required for TTX-induced synaptic enrichment of Shank3.** (A)

1184 Representative images of synaptic enrichment of endogenous Shank3 upon treatment with



1185 TTX and PP2A inhibitor fostriecin (FST) (scale bar = 10  $\mu$ m). (B) Quantification of synaptic  
1186 Shank3 intensity in (A) (number of neurons: DMSO, n = 26, FST, n = 28, TTX, n = 28,  
1187 TTX/FST, n = 29; Kruskal-Wallis test with post-hoc Dunn's tests: Un vs. FST, p > 0.9999,  
1188 DMSO vs. TTX, p = 0.0002 (\*\*\*), FST vs. TTX/FST, p = 0.1259, TTX vs. TTX/FST, p =  
1189 0.1292). (C) Quantification of density of synapses containing Shank3 in (A) (Kruskal-Wallis test  
1190 with post-hoc Dunn's tests: Un vs. FST, p = 0.9458, Un vs. TTX, p = 0.0051 (\*\*), FST vs.  
1191 TTX/FST, p = 0.2446, TTX vs. TTX/FST, p = 0.0273 (\*)). (D) Representative images of  
1192 synaptic enrichment of endogenous Shank3 upon treatment with TTX and PP1 inhibitor  
1193 tautomycetin (TAUT) (scale bar = 10  $\mu$ m). (E) Quantification of synaptic Shank3 intensity in (D)  
1194 (number of neurons: DMSO, n = 26, TAUT, n = 21, TTX, n = 28, TTX/TAUT, n = 32; Kruskal-  
1195 Wallis test with post-hoc Dunn's tests: DMSO vs. TAUT, p = 0.0315 (\*), DMSO vs. TTX, p =  
1196 0.0006 (\*\*\*), TAUT vs. TTX/TAUT, p = 0.0002 (\*\*\*), TTX vs. TTX/TAUT, p = 0.0392 (\*)). (F)  
1197 Quantification of density of synapses containing Shank3 in (D) (Kruskal-Wallis test with post-  
1198 hoc Dunn's tests: DMSO vs. TAUT, p = 0.2450, DMSO vs. TTX, p = 0.0116 (\*), TAUT vs.  
1199 TTX/TAUT, p = 0.6552, TTX vs. TTX/TAUT, p = 0.0007 (\*\*\*)).

1200

1201 **Figure 6. Changes in the phosphorylation state of Shank3 are crucial for bidirectional**  
1202 **synaptic scaling.** (A, B) Representative mEPSC recordings from neurons overexpressing  
1203 Shank3 WT (A) or DD mutant (B) during scaling up. (C) Quantification of average mEPSC  
1204 amplitude in (A) (WT, n = 8, WT+TTX, n = 9; unpaired two-tailed t test: p = 0.0074 (\*\*)). (D)  
1205 Quantification of average mEPSC amplitude in (B) (number of neurons: DD, n = 12, DD+TTX,  
1206 n = 14; unpaired two-tailed t test: p = 0.5708). (E, F) Representative traces of mEPSCs  
1207 recorded from neurons overexpressing Shank3 WT (E) or AA mutant (F) during scaling down.

1208 (G) Quantification of average mEPSC amplitude in (E) (number of neurons: WT, n = 8,  
1209 WT+BIC, n = 8; Mann-Whitney test: p = 0.0148 (\*)). (H) Quantification of average mEPSC  
1210 amplitude in (F) (AA, n = 9, AA+BIC, n = 14; unpaired two-tailed t test: p = 0.8612).

1211

1212 **Figure 7. Brief PP2A inactivation reverses scaling up.** (A) Representative images showing  
1213 the effects of 1 hr FST treatment on synaptic sGluA2 intensity in neurons expressing Shank3  
1214 WT or AA, after 24 hr of TTX to scale up synaptic strengths (scale bar = 10  $\mu$ m). (B)  
1215 Quantification of synaptic sGluA2 intensity in (A) (number of cells: WT/TTX, n = 22,  
1216 WT/TTX/FST, n = 23, AA/TTX, n = 26, AA/TTX/FST, n = 25; Mann-Whitney test: WT/TTX vs.  
1217 WT/TTX/FST, p = 0.0007 (\*\*\*), AA/TTX vs. AA/TTX/FST, p = 0.6337). (C) Quantification of  
1218 synaptic Shank3 intensity in (A) (Mann-Whitney test: WT/TTX vs. WT/TTX/FST, p = 0.0058  
1219 (\*\*), AA/TTX vs. AA/TTX/FST, p = 0.6204). In this experiment, WT/TTX/FST and AA/TTX/FST  
1220 were normalized to WT/TTX and AA/TTX, respectively.

1221

## 1222 SUPPLEMENTARY FIGURE LEGENDS

1223 **Figure 1 – Figure Supplement 1. Proteome and phosphoproteome dynamics in synaptic**  
1224 **signaling.** (A) Experimental workflow for deep proteome and phosphoproteome analysis of  
1225 cortical neuron explants treated with TTX or BIC. (B) Principal component analysis of the TTX  
1226 phosphoproteome dataset. (Left) Percent of variance explained by experimental factors in  
1227 each principal component. Most of the variance is explained by the biological replicate,  
1228 followed by the treatment time point. (Right) PCA plot shows grouping of replicates by  
1229 timepoint in dimensions 2 and 3. (C) Principal component analysis of the BIC  
1230 phosphoproteome dataset. (Left) Percent a variance explained by experimental factors in each

1231 principal component. Most of the variance is explained by the biological replicate, followed by  
1232 the treatment time point. (Right) PCA plot shows grouping of replicates by timepoint in  
1233 dimensions 2 and 3. (D) Heatmap showing the abundance (log<sub>2</sub> TMT ratios) of proteins with a  
1234 significant response to BIC treatment (F-test, adj.  $p < 0.1$ ). The gene symbols of the 27  
1235 regulated proteins are shown next to the heatmap.

1236

1237 **Figure 2 – Figure Supplement 1. Validation of the pS1615 antibody.** (A) Western blot  
1238 image showing the intensity of pS1615 in HA-tagged wild-type Shank3 or the S1586A/S1615A  
1239 (AA) mutant. One set of replicates were treated with the phosphatase inhibitor, okadaic acid  
1240 (OKA, 500 nM) for 30 minutes before lysis. Untr., untransfected control;  $n = 3$  biological  
1241 replicates. (B) Western blot image showing the intensity of pS1615 in HA-tagged wild-type  
1242 Shank3 with and without the treatment of lambda phosphatase ( $n = 4$  biological replicates).

1243

1244 **Figure 4 – Figure Supplement 1. PP1 regulates baseline phosphorylation of Shank3.** (A)  
1245 Western blot analysis showing changes in S1615 phosphorylation after 24-hr TTX treatment,  
1246 with PP1 inhibition by okadaic acid (OKA, 500 nM) during the last hour of the regimen. (B)  
1247 Quantification of S1615 phosphorylation in (A).

1248

1249 **Figure 5 – Figure Supplement 1. Inhibition of PP2A by OKA reverses TTX-induced**  
1250 **synaptic enrichment of Shank3.** (A) Representative images of synaptic enrichment of  
1251 endogenous Shank3 upon treatment with TTX and PP2A inhibitor OKA (50 nM, scale bar = 10  
1252  $\mu\text{m}$ ). (B) Quantification of synaptic Shank3 intensity in (A) (Un,  $n = 31$ , OKA,  $n = 29$ , TTX,  $n =$   
1253 30, TTX/OKA,  $n = 26$ ; Kruskal-Wallis test with post-hoc Dunn's tests: Un vs. OKA,  $p = 0.3286$ ,

1254 Un vs. TTX,  $p = 0.0002$  (\*\*\*), OKA vs. TTX/OKA,  $p > 0.9999$ , TTX vs. TTX/OKA,  $p = 0.0036$   
1255 (\*\*). (C) Quantification of density of synapses containing Shank3 in (A) (Kruskal-Wallis test  
1256 with post-hoc Dunn's tests: Un vs. OKA,  $p < 0.0001$  (\*\*\*\*), Un vs. TTX,  $p = 0.5125$ , OKA vs.  
1257 TTX/OKA,  $p > 0.9999$ , TTX vs. TTX/OKA,  $p < 0.0001$  (\*\*\*\*)).

1258

1259 **Figure 6 – Figure Supplement 1. Shank3 is required for synaptic scaling down. (A)**

1260 Quantification of average mEPSC amplitudes recorded from neurons depleted of Shank3.  
1261 Scaling down was induced by 24-hr treatment with PTX (CTNL,  $n = 19$ , PTX,  $n = 19$ , KD,  $n =$   
1262  $18$ , KD/PTX,  $n = 16$ ; Mann-Whitney test: CTNL vs. PTX,  $p = 0.0233$  (\*), KD vs. KD/PTX,  $p =$   
1263  $0.8515$ ). (B) Cumulative histogram of mEPSC amplitudes (two-sample Kolmogorov-Smirnov  
1264 test: CTNL vs. PTX,  $p = 0.0017$  (\*\*), PTX vs. KD/PTX,  $p = 0.0624$ , CTNL vs. KD/PTX,  $p =$   
1265  $0.0945$ ).

1266

1267 **Figure 6 – Figure Supplement 2. Scaling up and down remain intact in neurons**

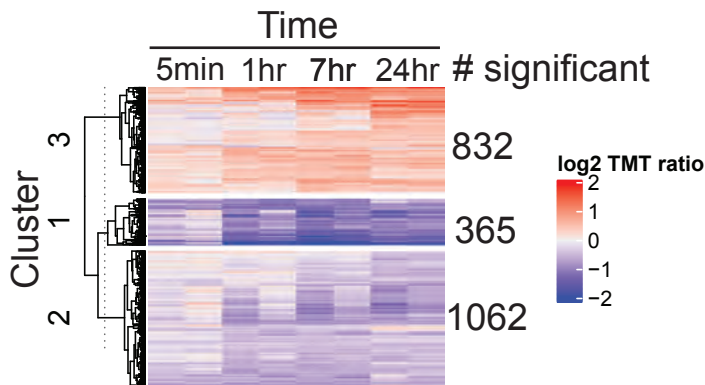
1268 **overexpressing Shank3 AA and DD, respectively. (A)** Representative images of changes in  
1269 synaptic sGluA2 intensity in neurons overexpressing Shank3 WT and AA during scaling up  
1270 (scale bar =  $10 \mu\text{M}$ ). (B) Quantification of average synaptic sGluA2 intensity in (A) (WT,  $n = 28$ ,  
1271 WT/TTX,  $n = 30$ , AA,  $n = 34$ , AA/TTX,  $n = 28$ ; Mann-Whitney test: WT vs. WT/TTX,  $p = 0.0009$   
1272 (\*\*\*), AA vs. AA/TTX,  $p = 0.0013$  (\*\*)). (C) Representative images of changes in synaptic  
1273 sGluA2 intensity in neurons overexpressing Shank3 WT and DD during scaling down (scale  
1274 bar =  $10 \mu\text{M}$ ). (D) Quantification of average synaptic sGluA2 intensity in (C) (WT,  $n = 41$ ,  
1275 WT/BIC,  $n = 45$ , DD,  $n = 29$ , DD/BIC,  $n = 30$ ; Mann-Whitney test: WT vs. WT/BIC,  $p = 0.0230$   
1276 (\*), DD vs. DD/BIC,  $p = 0.0300$  (\*)).

# Figure 1

bioRxiv preprint doi: <https://doi.org/10.1101/2021.10.03.462942>; this version posted October 3, 2021. The copyright holder for this preprint (which was not certified by peer review) is the author/funder, who has granted bioRxiv a license to display the preprint in perpetuity. It is made available under aCC-BY 4.0 International license.

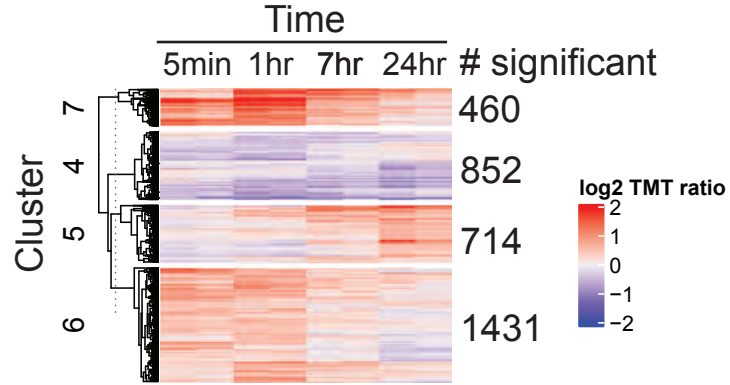
A

## Significant phosphosites in TTX treatment



B

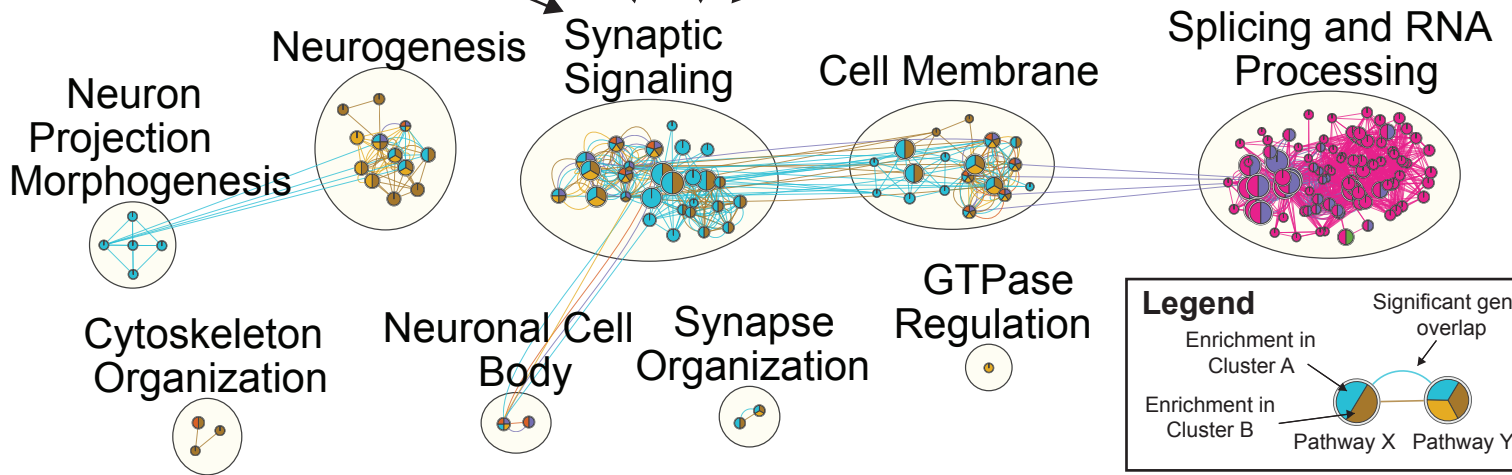
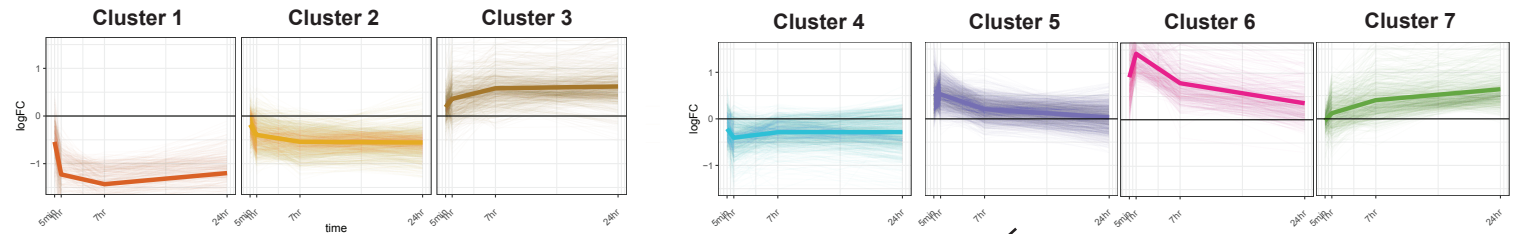
## Significant phosphosites in BIC treatment



C

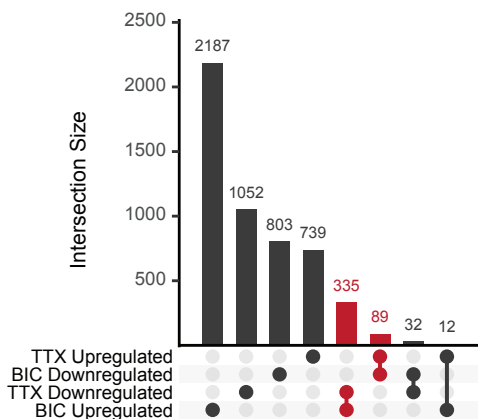
## TTX phospho cluster profile

## BIC phospho cluster profile



D

## Sig. phosphosites TTX and BIC



E

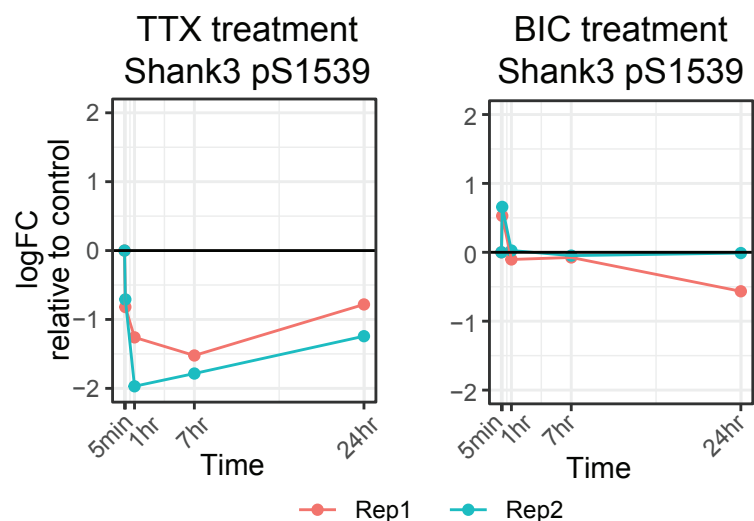
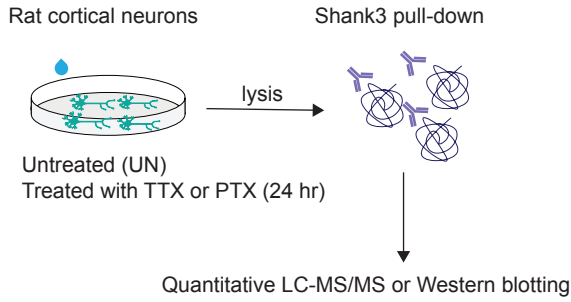


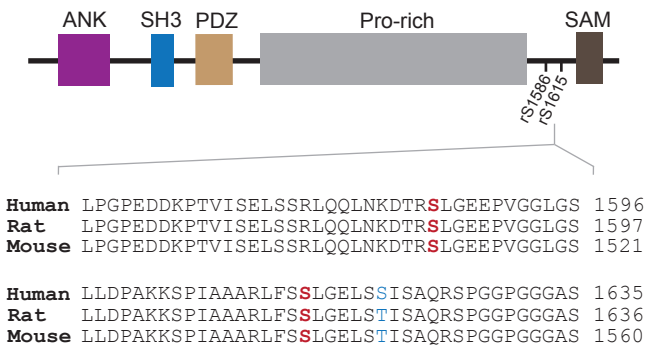
# Figure 2

bioRxiv preprint doi: <https://doi.org/10.1101/2021.10.03.462942>; this version posted October 3, 2021. The copyright holder for this preprint (which was not certified by peer review) is the author/funder, who has granted bioRxiv a license to display the preprint in perpetuity. It is made available under aCC-BY 4.0 International license.

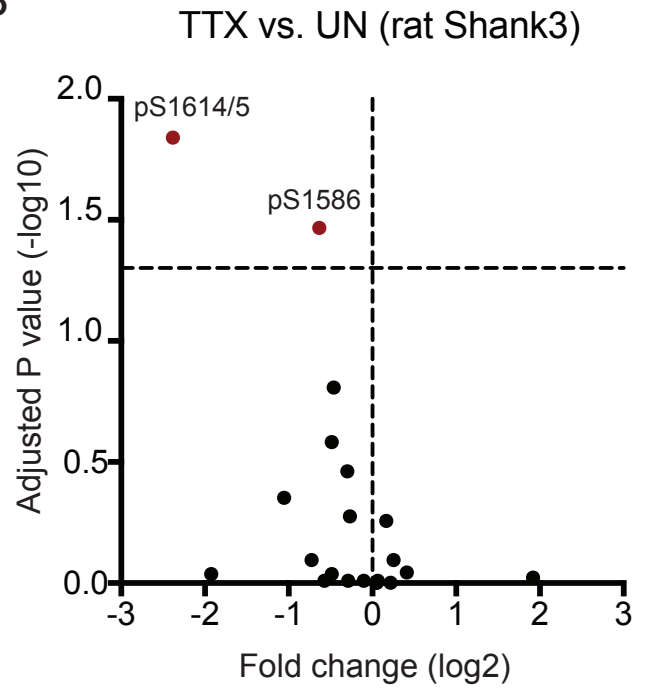
**A**



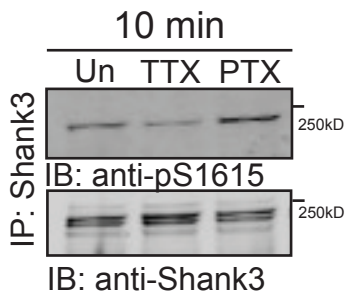
**C**



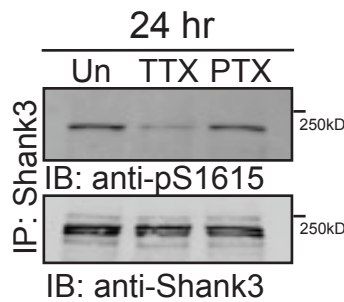
**B**



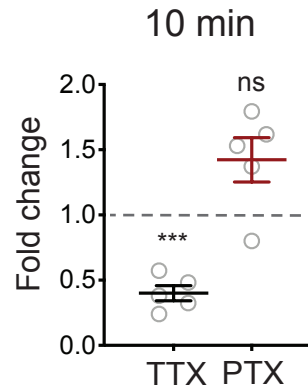
**D**



**E**



**F**



**G**

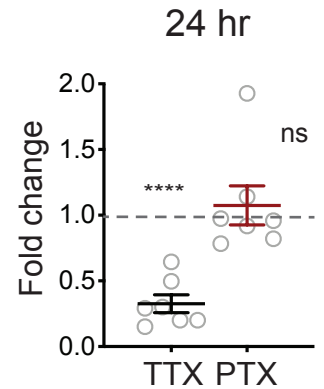


# Figure 3

bioRxiv preprint doi: <https://doi.org/10.1101/2021.10.03.462942>; this version posted October 3, 2021. The copyright holder for this preprint (which was not certified by peer review) is the author/funder, who has granted bioRxiv a license to display the preprint in perpetuity. It is made available under aCC-BY 4.0 International license.

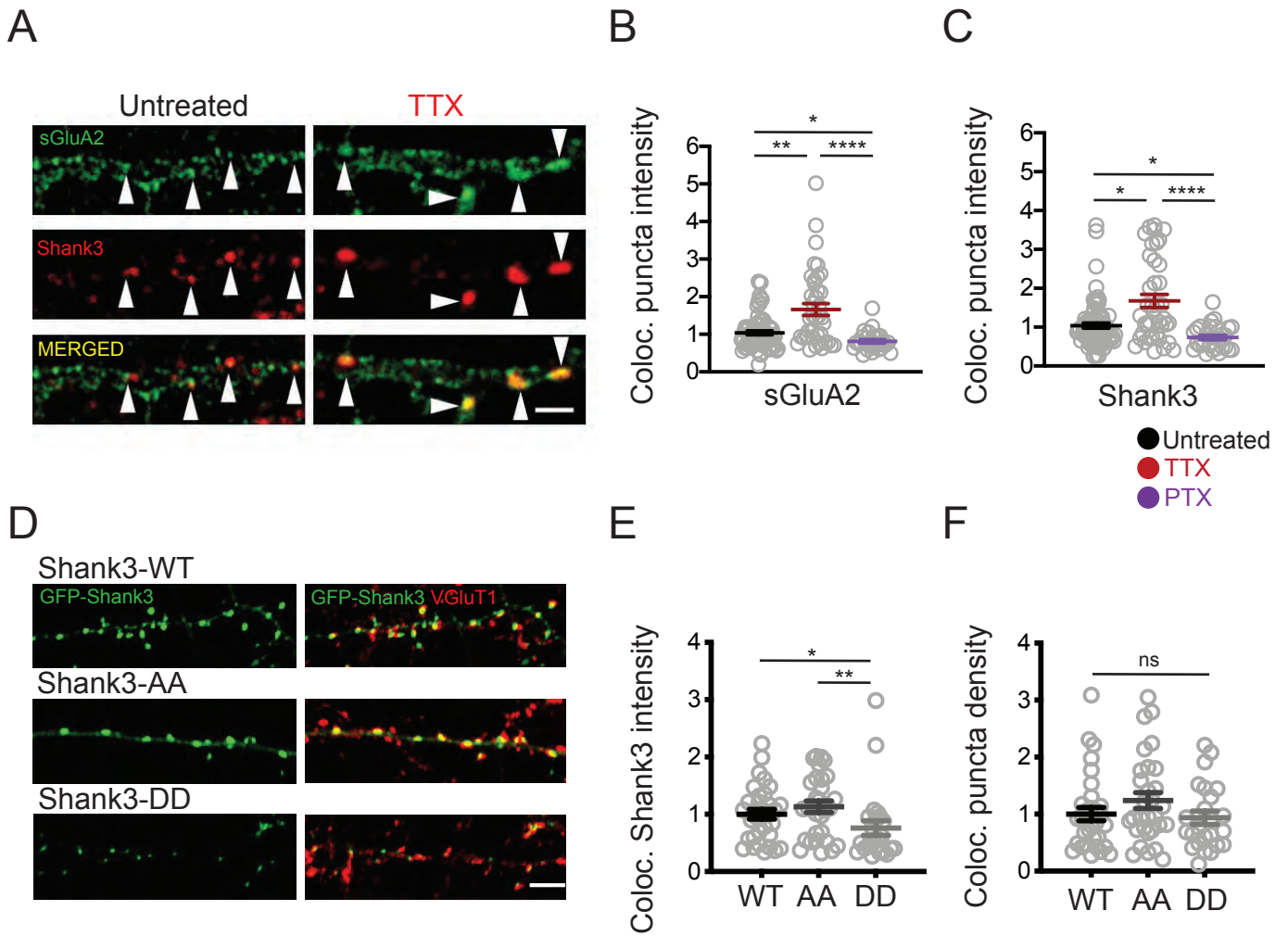




# Figure 4

bioRxiv preprint doi: <https://doi.org/10.1101/2021.10.03.462942>; this version posted October 3, 2021. The copyright holder for this preprint (which was not certified by peer review) is the author/funder, who has granted bioRxiv a license to display the preprint in perpetuity. It is made available under a [CC-BY 4.0 International license](https://creativecommons.org/licenses/by/4.0/).

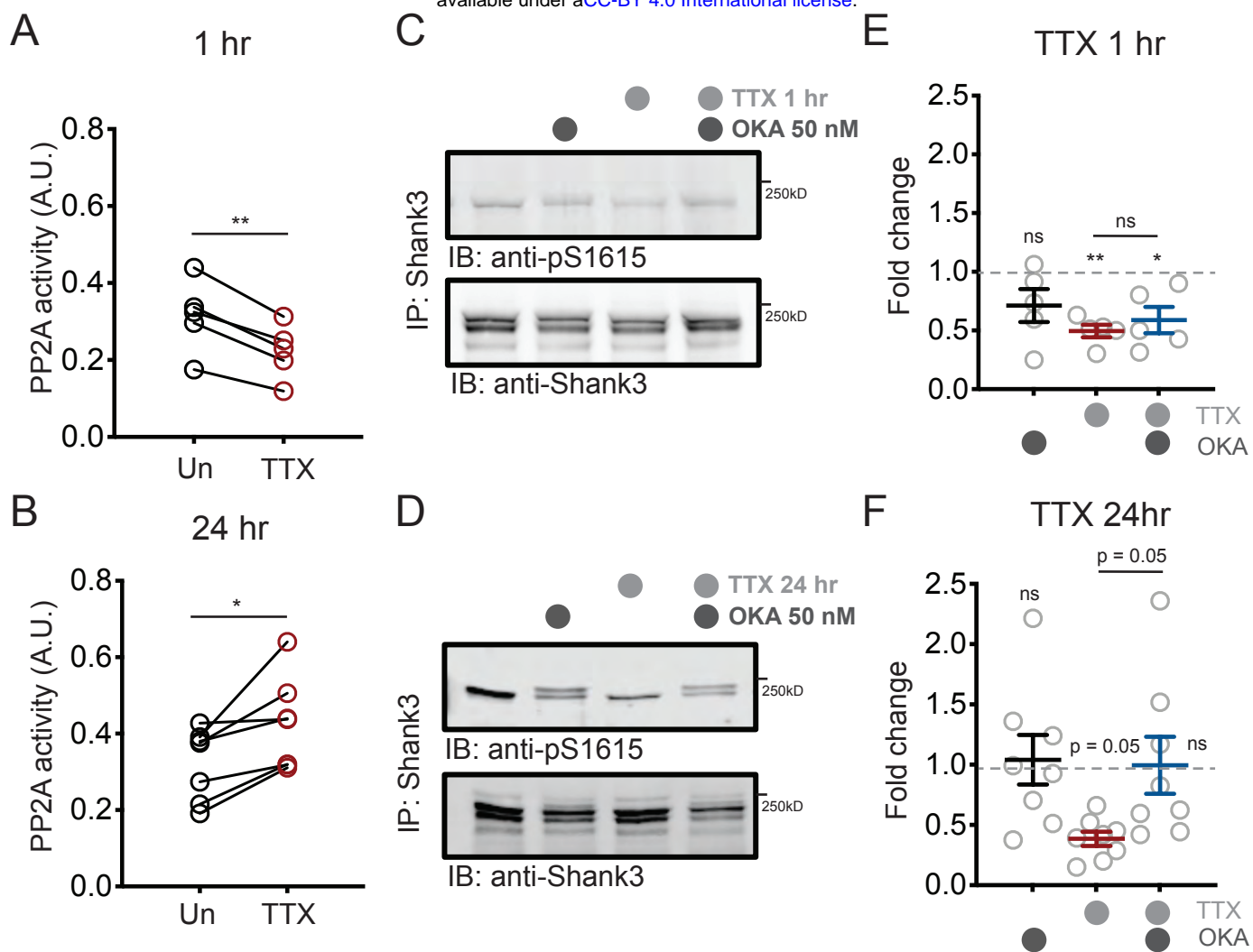


# Figure 5

bioRxiv preprint doi: <https://doi.org/10.1101/2021.10.03.462942>; this version posted October 3, 2021. The copyright holder for this preprint (which was not certified by peer review) is the author/funder, who has granted bioRxiv a license to display the preprint in perpetuity. It is made available under aCC-BY 4.0 International license.

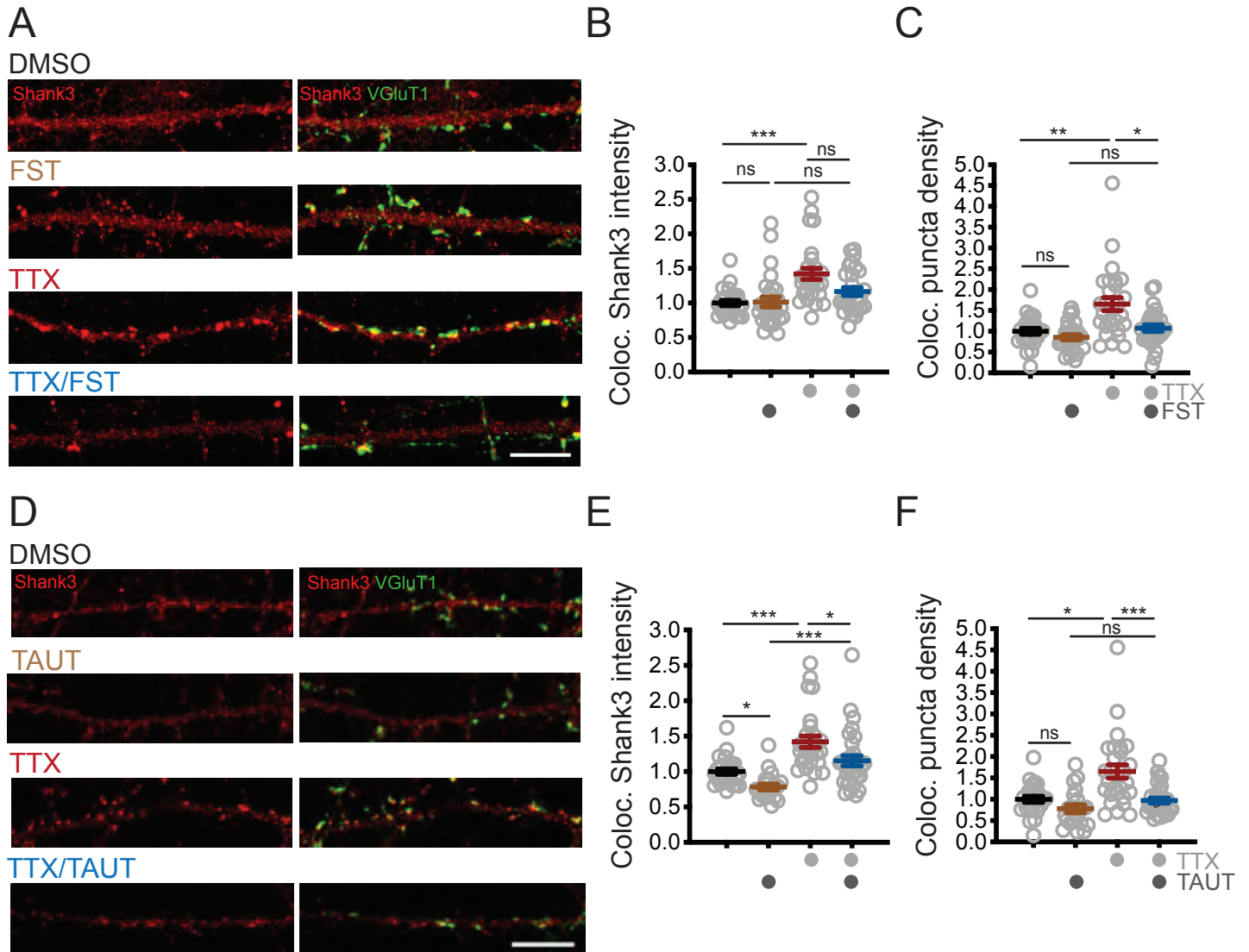


# Figure 6

bioRxiv preprint doi: <https://doi.org/10.1101/2021.10.03.462942>; this version posted October 3, 2021. The copyright holder for this preprint (which was not certified by peer review) is the author/funder, who has granted bioRxiv a license to display the preprint in perpetuity. It is made available under a [CC-BY 4.0 International license](https://creativecommons.org/licenses/by/4.0/).

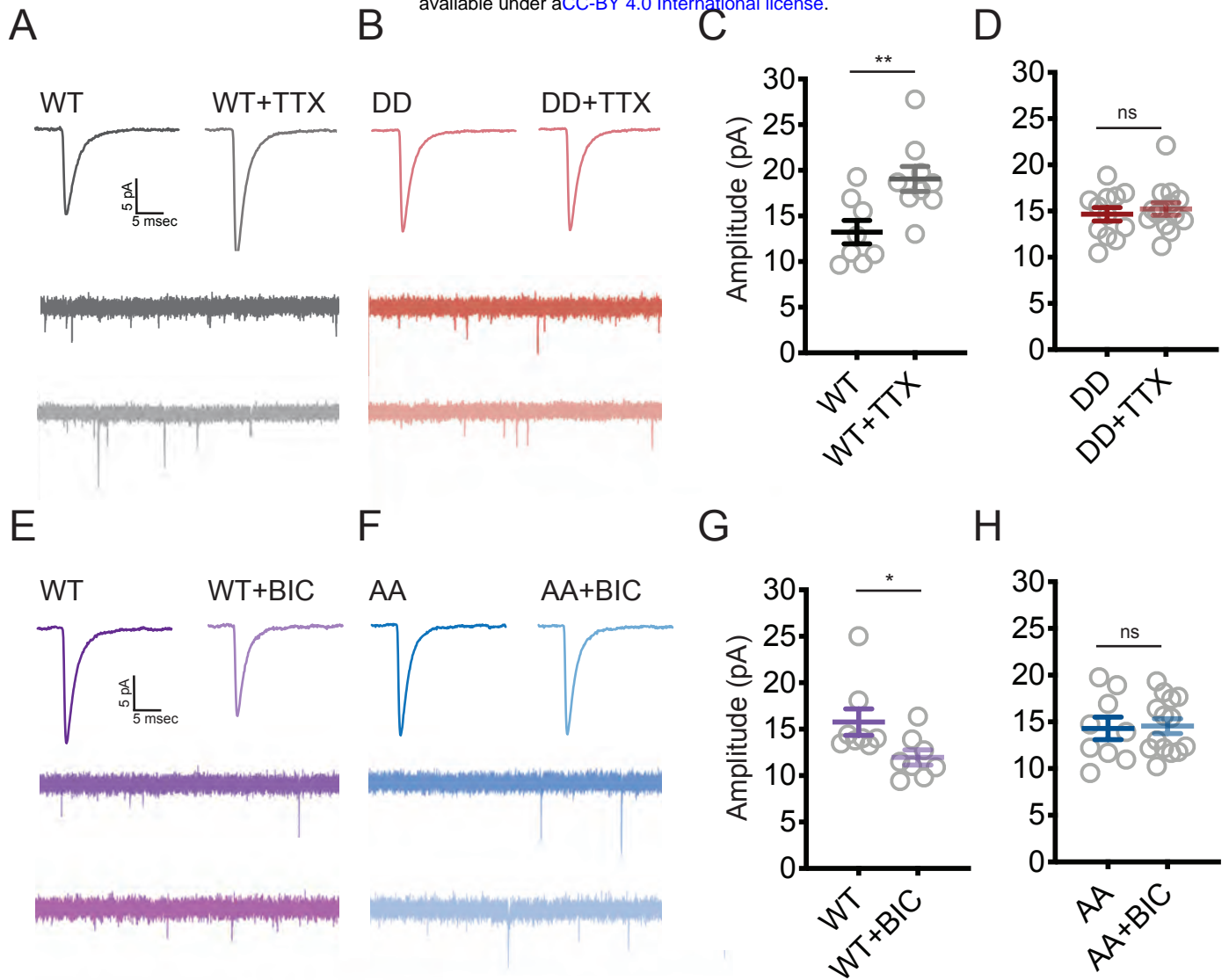
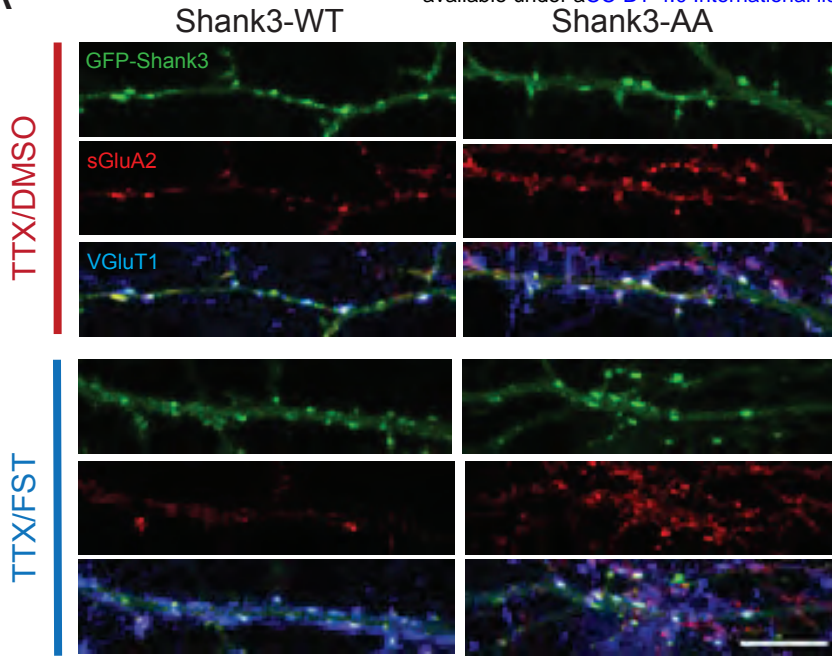


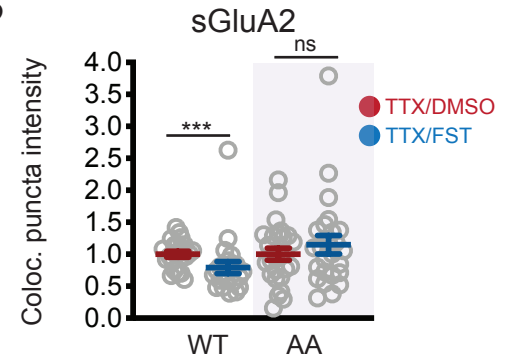
# Figure 7

bioRxiv preprint doi: <https://doi.org/10.1101/2021.10.03.462942>; this version posted October 3, 2021. The copyright holder for this preprint (which was not certified by peer review) is the author/funder, who has granted bioRxiv a license to display the preprint in perpetuity. It is made available under a [CC-BY 4.0 International license](#).

A



B



C

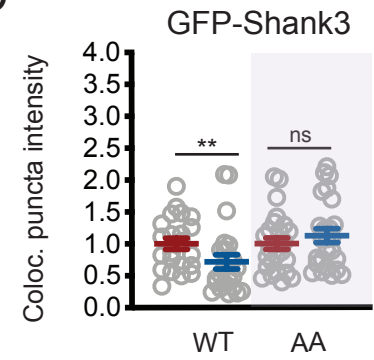


# Figure 1 — figure supplement 1

bioRxiv preprint doi: <https://doi.org/10.1101/2021.10.03.462942>; this version posted October 3, 2021. The copyright holder for this preprint (which was not certified by peer review) is the author/funder, who has granted bioRxiv a license to display the preprint in perpetuity. It is made available under aCC-BY 4.0 International license.

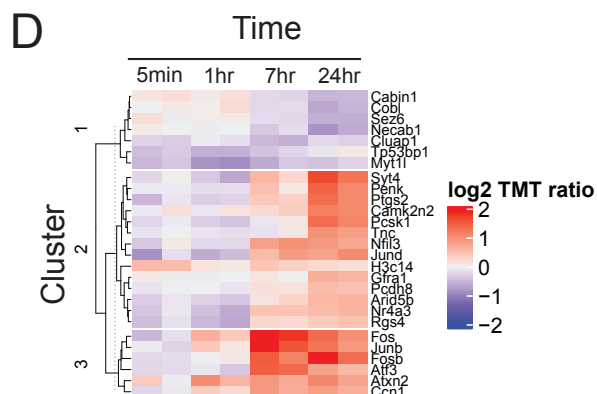
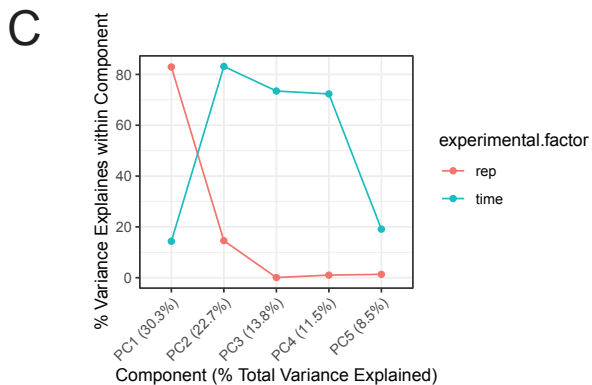
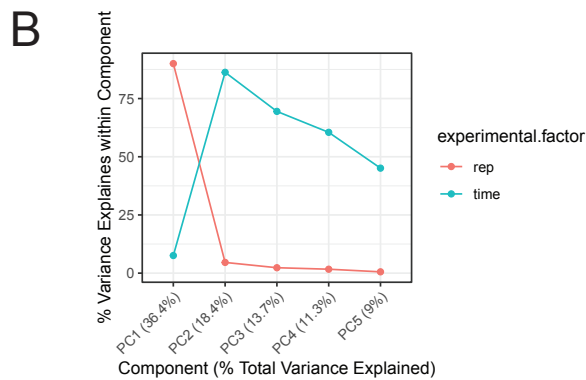
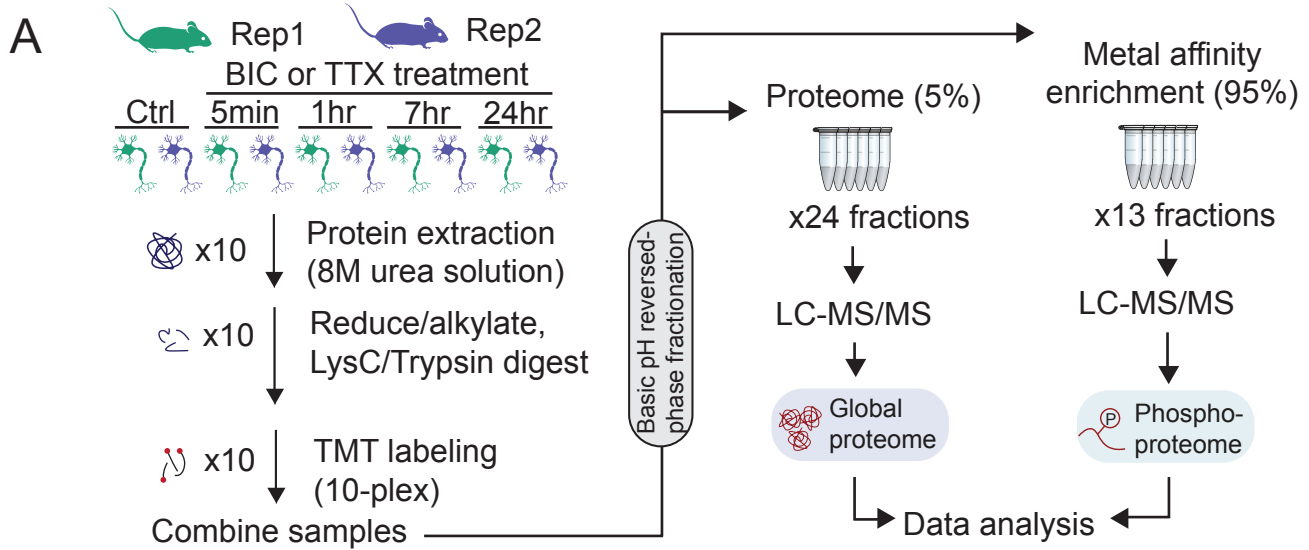
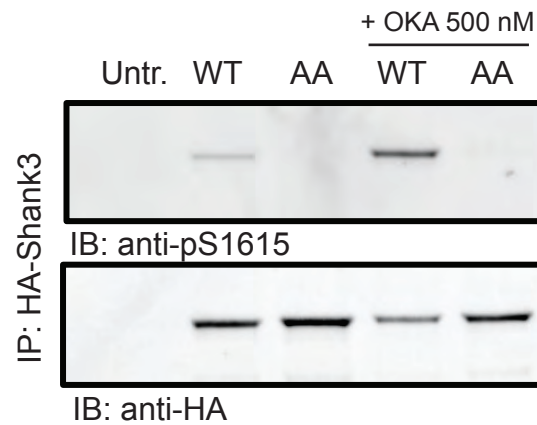


# Figure 2 — figure supplement 1

bioRxiv preprint doi: <https://doi.org/10.1101/2021.10.03.462942>; this version posted October 3, 2021. The copyright holder for this preprint (which was not certified by peer review) is the author/funder, who has granted bioRxiv a license to display the preprint in perpetuity. It is made available under a [CC-BY 4.0 International license](#).

A



B

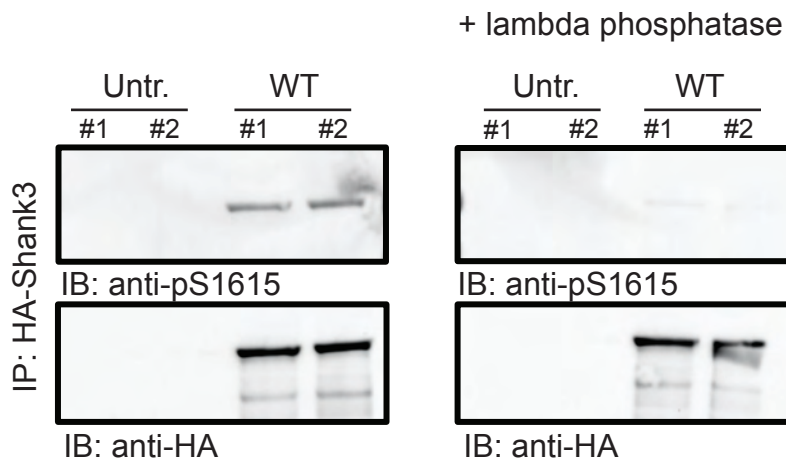
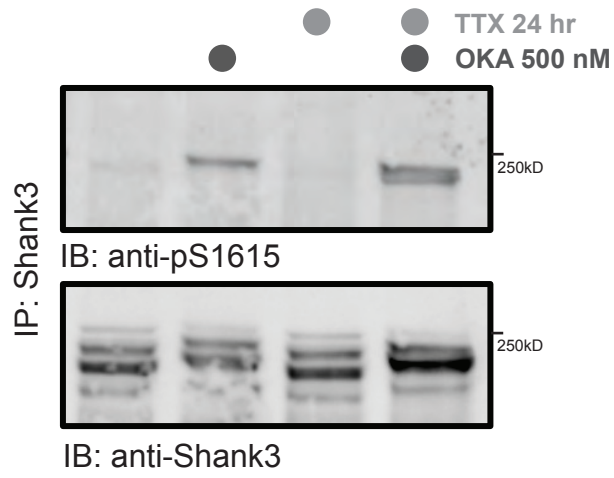


# Figure 4 — figure supplement 1

bioRxiv preprint doi: <https://doi.org/10.1101/2021.10.05.462942>; this version posted October 3, 2021. The copyright holder for this preprint (which was not certified by peer review) is the author/funder, who has granted bioRxiv a license to display the preprint in perpetuity. It is made available under a [CC-BY 4.0 International license](https://creativecommons.org/licenses/by/4.0/).

A



B

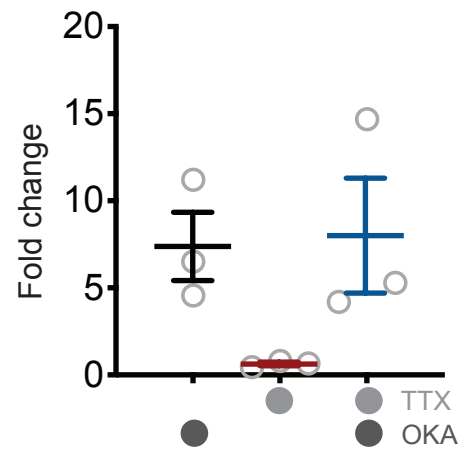
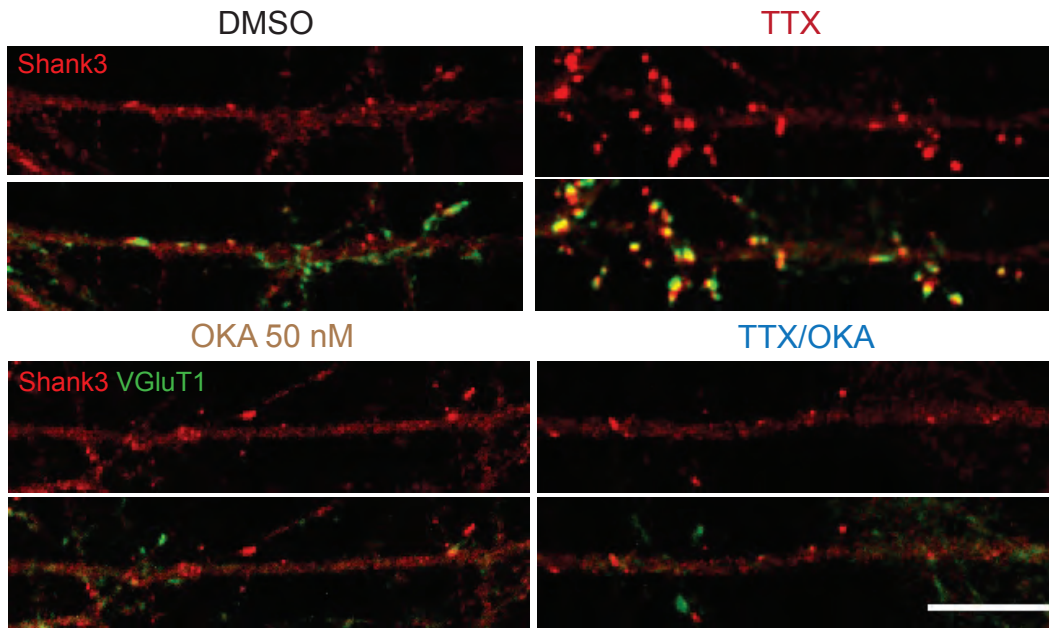




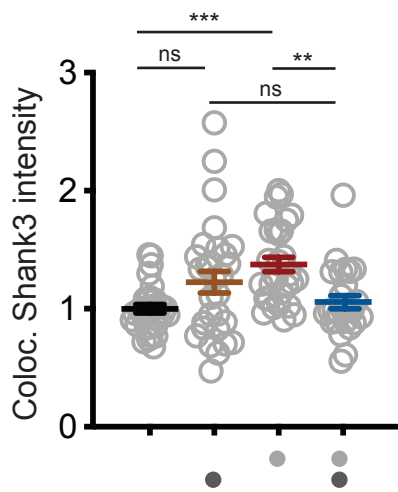
# Figure 5 — figure supplement 1

bioRxiv preprint doi: <https://doi.org/10.1101/2021.10.03.462942>; this version posted October 3, 2021. The copyright holder for this preprint (which was not certified by peer review) is the author/funder, who has granted bioRxiv a license to display the preprint in perpetuity. It is made available under aCC-BY 4.0 International license.

A



B



C

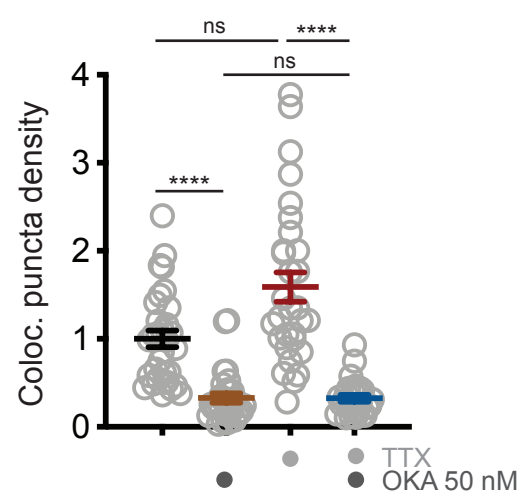
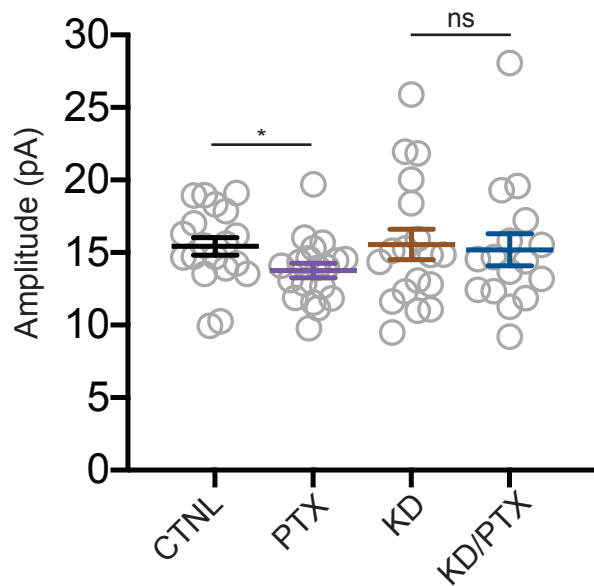


# Figure 6 — figure supplement 1

bioRxiv preprint doi: <https://doi.org/10.1101/2021.10.03.462942>; this version posted October 3, 2021. The copyright holder for this preprint (which was not certified by peer review) is the author/funder, who has granted bioRxiv a license to display the preprint in perpetuity. It is made available under a [CC-BY 4.0 International license](#).

A



B

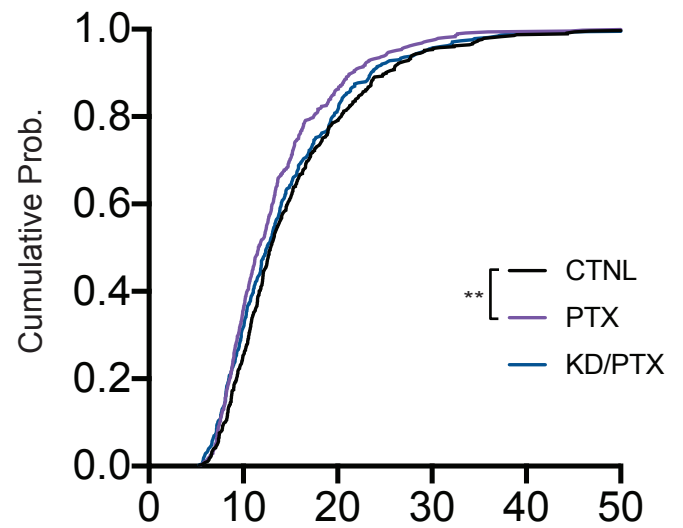


# Figure 6 — figure supplement 2

bioRxiv preprint doi: <https://doi.org/10.1101/2021.10.03.462942>; this version posted October 3, 2021. The copyright holder for this preprint (which was not certified by peer review) is the author/funder, who has granted bioRxiv a license to display the preprint in perpetuity. It is made available under aCC-BY 4.0 International license.

